SOUNDSCAPE CHARACTERIZATION IN GRAND PASSAGE, NOVA SCOTIA, A PLANNED IN-STREAM TIDAL ENERGY SITE

by

Anne Lombardi

Submitted in partial fulfillment of the requirements
for the degree of Master of Science

at

Dalhousie University
Halifax, Nova Scotia
December 2016

Dedicated to the eternal and persistent pursuit of a respectful, gracious, and harmonious relationship between humans and the natural world. And to my eternal companion Derek, whose sound disposition gives me the power to stay afloat when I've drifted to the wrong end of the spectrum.

TABLE OF CONTENTS

LIST OF TABLES

LIST OF FIGURES

ABSTRACT

The marine environment in the Bay of Fundy hosts a dynamic and diverse soundscape that is a fundamental component of the local ecosystem. The emergence of new human marine activities and infrastructure, such as tidal turbine installations, introduces new sound sources that change or disrupt the existing acoustic environment, but the full extent of these changes is not well understood and is not predictable. To better evaluate the effects of future tidal energy development on the local soundscape in Grand Passage, Nova Scotia, a thorough understanding of the pre-development characteristics must be established. The present research seeks to identify existing anthropophony, biophony, and geophony, and to evaluate the underlying mechanisms contributing to geophonic variability.

LIST OF ABBREVIATIONS AND SYMBOLS USED

Roman symbol	Description	Units
a	Radius	m
c	Sound speed	m/s
C_d	Drag coefficient	Dimensionless
d	Hydrophone array spacing	m
D	Diameter	m
E	Young's modulus of elasticity	Pa
f	Frequency	Hz
g	Gravity	m/s^2
h	Depth below surface	m
k	Wavenumber	rad/m
K	Degrees of freedom	Dimensionless
l	Distance between sound source and image	m
L	Largest hydrophone dimension	m
P	Pressure	Pa
t	Time	s
u_*	Friction velocity	m/s
U	Mean flow speed	m/s
z	Height above bed	m
CSD	Cross Spectral Density	dB re 1 μPa^2/Hz
PSD	Pressure Spectral Density	dB re 1 μPa^2/Hz
SGN	Sediment Generated Noise	dB re 1 μPa
SNR	Signal to Noise Ratio	Dimensionless
SPL	Sound Pressure Level	dB re 1 μPa

Greek symbol	Description	Units
β	Slope of PSD curve	dB re μPa^2/Hz^2
γ	Ratio of specific heats	Dimensionless
Γ^2	Magnitude squared coherency	Dimensionless
ϵ	Turbulence dissipation rate	m^2/s^3
ε	Error	Relative
η_0	Kolmogorov microscale	mm
θ	Source angle	Radians/Degrees
θ_c	Shield's parameter	Dimensionless
κ	von Karman's constant	Dimensionless
λ	Wavelength	m
ρ	density of water	kg m^{-3}
ρ_s	density of sediment	kg m^{-3}
σ	Poisson's ratio	Dimensionless
τ_0	Critical bed shear stress	Pa
ϕ	Phase	Dimensionless
ω	Angular frequency	radians/s

ACKNOWLEDGEMENTS

Countless members of our local oceanography and marine engineering community provided assistance and guidance over the course of this research, and I am grateful for the contributions and honoured to have worked within such a supportive research environment. In particular, I wish to acknowledge the guidance of my supervisors Alex Hay and David Barclay, who supported my pursuit of what might be an "unconventional" approach to graduate research in the physical oceanography field, and accommodated a not insignificant amount of floundering from an engineer masquerading as a physicist. In addition, I'd like to thank those who contributed directly to data collection and analysis:

Richard Cheel
Justine McMillan
Greg Trowse
Chris Loadman
Captain and crew of the *MV Nova Endeavour* and RHIB operator Reid Gillis

And finally, I'd like to acknowledge the funding sources for this research:

NSERC Industrial Postgraduate Scholarship Program
NRCan ecoEnergy Program
Fundy Tidal Inc.

CHAPTER 1

INTRODUCTION

1.1 The "Soundscape" and ambient noise

The term "ambient noise" is often used to describe the sound levels that exist in the absence of any identifiable sources, originally without directional information, but more recently expanded to also include directional distribution of ambient levels. The terminology is loosely defined, hindering accurate comparisons between specific studies. Recently, much of the sound research literature has adopted "soundscape" terminology, a concept that was originally introduced by R. Murray Schafer in 1977 (*Krause*, 2008); associated terminology, including biophony (biological sounds), geophony (sounds associated with the natural physical environment), and anthropophony (sounds associated with human activity), have also been adopted, and will be used within this thesis.

The term "soundscape" is now defined as the "acoustic environment as perceived or experienced and/or understood by a person or people, in context" in the ISO standard for soundscapes (ISO 12913-1:2014) (*ISO*, 2014). The standard was developed in response to inconsistency in the use of soundscape terminology in different fields and applications, and seeks to provide a foundation for comparison across disciplines; in facilitating this comparision, the standard also provides definition and scope for measurement approaches and presentation of data. Through analysis of acoustic measurements obtained using appropriate methodologies, properties of the acoustic environment or noise field can be evaluated, from which the soundscape characteristics can be derived.

As evidenced by the increased research focus on soundscapes and the role of sound in marine ecosystems (e.g. *Williams et al.*, 2014; *Erbe et al.*, 2015), many traditional baseline noise concepts and measurement approaches do not sufficiently address the variability in

underlying sound production and propagation mechanisms that ultimately govern the local acoustic environment. For example, baseline acoustic surveys, conducted within the scope of an environmental assessment for marine infrastructure development, may present results in terms of mean, minimum, and maximum third-octave band (TOB) levels at a particular location; a summary of such studies related to marine renewable energy development is provided by *Robinson and Lepper* (2013).

As identified in the Robinson and Lepper review, these methods do not provide an appropriate context for quantitative comparison of results, as the acoustic surveys varied in duration, season, weather conditions, and deployment methods, and the inclusion of supplementary datasets such as flow speed was limited in many cases. In addition, such techniques do not promote adaptive measurement methods that acknowledge and utilize the environmental conditions. Alternatively, the soundscape approach provides a compilation of various features that systematically represent a complex, dynamic acoustic environment; by identifying biological, environmental, and anthropogenic sound sources, the soundscape methodology inherently acknowledges and addresses the influence of a unique local environment, enabling a more comprehensive understanding of the existing conditions.

1.2 Background and Motivation

The conversion of kinetic energy from tidal flows into electrical energy has recently become a reality, with the installation of tidal energy turbines in the UK, France and several planned installations in the Bay of Fundy. The introduction of in-stream tidal energy conversion (TEC) devices into the marine environment can have an impact on local environmental characteristics, such as flow dynamics, seabed properties, benthic organisms, and marine mammals. As the industry progresses, continued research is necessary to ensure that any such impacts are known and actively minimized, and that environmental changes are effectively monitored over time.

Underwater noise associated with tidal energy, including noise from turbines and mooring infrastructure as well as noise from construction/maintenance, has potential implications for marine mammals that use sound for communication or navigation, and for other organisms that may be negatively impacted by increased acoustic energy and/or pressure levels and particle motion. In addition, the source level and transmission of

TEC-generated noise has implications for both the detection of hazards by marine life and for local marine mammal monitoring through passive acoustics. To quantify the noise introduced by tidal energy activities, and to assess its effects on the local environment, knowledge of pre-development baseline conditions must be established.

However, soundscape characterization in areas suitable for tidal energy is inherently challenging due to (1) pseudonoise contamination from turbulent flows; (2) increased broadband noise from mobile sediments in bedload motion or saltation; (3) variability of sound sources in coastal and near-coastal regions; and (4) complexity of propagation regimes in shallow water environments. The approach, including both instrumentation and analysis, must therefore address these challenges through mitigation of contamination effects and evaluation of noise over a broad range of frequencies, timescales, and spatial dimensions.

With high flow speeds and shallow bathymetry, the marine environment in Grand Passage (and nearby tidal channels Petit Passage and Digby Gut) has high potential for small scale tidal energy development (*Hay et al.*, 2013a); all three passages have been granted a tidal power development license by the Nova Scotia government. The strong flows in the Bay of Fundy provide not only a renewable energy resource, but also provide a dynamic, nutrient-rich ecosystem that supports a variety of marine organisms, which in turn hosts several active fisheries and attracts significant levels of recreational traffic from whale watching activities. Geographically, the outer Bay of Fundy provides marine access to several ports and local wharves, including the port of Saint John, New Brunswick.

The soundscape throughout the Bay is thus complex and dynamic, with a significant anthropophonic contribution from vessel traffic and a diverse biophonic contribution from marine mammals; within the Grand Passage environment, this complexity is amplified by the channel geometry, concentrated anthropogenic activity, and elevated current speeds.

1.3 Objectives

The present research seeks to address important knowledge gaps related to noise sources in Grand Passage. Specifically,

- What are the current levels and sources of ambient noise in Grand Passage, and how dominant is the sediment-generated noise (SGN) contribution?
- How do local physical, biological, and anthropogenic conditions influence the observed soundscape?
- What are the potential acoustic impacts of tidal energy development, in relation to the existing soundscape?

To develop an improved understanding of the local acoustic environment and soundscape, and thus provide a foundation for effective long term passive acoustic monitoring and acoustic impact assessment, the research focused on the following objectives:

1. Characterize the existing soundscape based on geophonic, biophonic, and anthropophonic contributors
2. Evaluate spatial and temporal variability in soundscape geophony and identify mechanisms of sound production

1.4 Thesis Organization

Relevant information and theory related to underwater acoustics and soundscapes is provided in chapter 2. The research approach, including instrumentation used and analysis methods, is described in chapter 3. The soundscape characteristics derived from the research results are discussed in chapter 4. Variability in the soundscape geophony due to influence of high-energy weather events is evaluated and discussed in chapter 5. A summary of the research and major conclusions is provided in chapter 6.

The units of sound pressure levels (SPLs) and pressure spectral density (PSD) used in this thesis are dB re 1 μPa and dB re 1 μPa^2/Hz, respectively. For the remainder of this document, these have been abbreviated to dB re μPa and dB re μPa^2/Hz.

CHAPTER 2

THEORY AND BACKGROUND

2.1 Sound Propagation

The propagation of sound sources in a tidal channel has a significant effect on soundscape characteristics. With a shallow and narrow geometry, the propagation of acoustic energy is subject to significantly more bottom interactions as compared to the open ocean; when a source interacts with the bottom, sound waves are affected by reflection/transmission or scattering, both of which will result in lower energy at the receiver. However, the shallow water environment can also act as an acoustic waveguide, whereby sound waves become "trapped" in a channel bounded by the surface and bottom interfaces, reducing transmission loss at short ranges as energy that would otherwise be lost to spreading is reflected back into the channel. Given the various physical characteristics contributing to these processes, the quantitative effects in a real environment are difficult to predict. Qualitatively, sound sources measured by a receiver may be either lost or distorted, depending on signal duration, intensity, frequency, bottom type, depth, and range. Short sound pulses, like the clicks made by some marine mammals, can be distorted by a combination of bottom interaction processes, transforming a short pulse into what has been described as a "drawn-out blob" (*Urick*, 1979), due to the dispersive nature of the acoustic channel through the waveguide. Attenuation by bottom materials is greater for higher frequency waves, and energy can be lost before the wave reaches the receiver. Bottom roughness can cause scattering and loss of wave intensity. Reflectivity of both surface and bottom boundaries influences the horizontal symmetry of the local noise field, and can amplify or reduce coherent sound intensity through constructive and destructive interference of source images.

2.1.1 Normal Modes and Ray Theory

Two main theoretical models exist to describe the propagation of sound between a source and receiver in shallow water, namely the Normal Mode theory and Ray theory. Normal mode theory is based on an exact infinite summation of waves each propagating with a depth-dependent amplitude in accordance with the related Hankel function for a particular wavenumber. A variety of solutions exist to represent various propagation regimes; one such solution, the Pekeris waveguide, introduces an infinite fluid bottom, with a flat, horizontal interface, into which energy can be transmitted and thus lost from the water column (*Jensen et al.*, 2011).

A defining characteristic of the normal mode is the existence of a cutoff frequency, which is the lowest frequency for a given mode number (m), below which waves cannot propagate horizontally. In the Pekeris waveguide, this is represented as follows:

$$f_{0m} = \frac{(m - 0.5)c_w c_b}{2h\sqrt{c_b^2 - c_w^2}} \tag{2.1}$$

where c_w is the sound speed in water, c_b is the sound speed in the bottom, and h is the depth. The cutoff frequency is higher in shallow water, which has implications for low frequency propagation in a tidal channel; with $c_b = 1800$ m/s, $c_w = 1500$ m/s, and $h = 20$ m, f_{0m} =34, 102, and 170 Hz for modes 1-3.

Ray theory describes sound wave propagation through the movement of wavefronts along ray paths. This approach provides a better visual representation of acoustic waves through ray diagrams, but is limited to cases where changes in velocity or pressure amplitude occur only over distances greater than one wavelength; typically, this constrains ray models to high frequency applications (*Urick*, 1979). Ray theory, and specifically Snell's law, can also describe the transformation of wave fronts between layers of different sound velocities. In a shallow, high flow tidal channel, however, the water column is typically well mixed and sound speed gradients are minimal, so the applicability of Snell's law is limited to a case where refraction due to current shear is important.

Ray paths can provide a useful interpretation of sound propagation in shallow water, as a source and its various reflections can each be represented by individual paths. With a source at a given distance from a receiver, in a medium having boundaries at the surface and bottom, the received signal becomes an infinite summation of the original source and

images of the source, each added to satisfy the boundary conditions. At increasing range, the higher order images decrease with $1/r_n$, where r_n is the distance from receiver of the n^{th} source image. It follows, therefore, that ray theory best describes propagation at short ranges.

The applicability of mode or ray theory within a given environment is typically differentiated by frequency and depth, with normal mode theory being better suited to shallow water (for both low and high frequency) and ray theory better suited to high frequencies or where there is relatively small change in c over a wavelength (or $kd \gg 1$) (*Urick*, 1983). In Grand Passage, with shallow depths (see figure 3.1) and an unstratified water column (due to turbulent mixing), both theories are appropriate for the frequencies of interest in this research; with minimum depths of 10 m, $kd \gg 1$ for $f > 1$ kHz.

2.2 Anthropophony

The anthropophonic contribution to ocean soundscapes is largely comprised of sources from vessels, but also includes other man-made sounds such as drilling, geophysical surveys, or marine construction. In the context of this research, the most relevant anthropogenic sound sources are vessel noise and TEC device noise. In addition, non-acoustic pseudonoise can be considered a component of the anthropophony, as it results from anthropogenic measurement of the sound field (see section 2.2.3).

2.2.1 Vessel noise

The noise contribution from propellor-driven vessels has been separated in the literature between traffic noise, referring to a compilation of ship sources creating an ambient, constant source, and ship noise, referring to sounds generated from individual vessels. In shallow water, traffic noise has little relevance due to propagation regimes and proximity to major shipping lanes with constant noise. Instead, intermittent ship noise can produce high local levels that are important in a site specific context. This type of vessel noise has been shown to be predominantly concentrated in low frequencies, with noise from rotating machinery dominant and electrical components (at 60 Hz) below 1 kHz and noise from water movement around the vessel dominant above 1 kHz, to an upper detectable limit around 20 kHz (*Richards et al.*, 2007). These values and related SPLs are dependent on a variety of vessels-specific factors such as speed or propeller size, making boat noise an

unpredictable and inconsistent contributor to the local soundscape.

2.2.2 TEC device noise

TEC devices introduce noise into the environment through both interactions with the flow regime, in the form of inflow turbulence and cavitation, and through "self noise", in the form of vortex shedding and trailing edge eddy convection (*Lloyd et al.*, 2011). While most of these phenomena generate broadband noise, vortex shedding can generate high tonal SPLs at frequencies related to trailing edge shape. These various sources also have associated directionality, which has implications for the potential marine mammal response to, and ability to detect, operating turbines. A detailed discussion of the processes involved in the generation of turbine noise is beyond the scope of this research; however, it is important to note that source noise levels and bandwidths are related to device design and flow characteristics, thus field measurements of noise are currently a suitable means of quantifying operational noise due to a particular device at a particular site. In addition to regular operation noise, sound can be generated by faulty components such as loose bearings or broken parts. These would represent random, non-characteristic sources that would further increase the device's acoustic impact in the soundscape.

Despite the complexity and variability of factors contributing to turbine-generated noise, there have been recent efforts to model potential turbine sound generated from two particular processes: device interaction with inflow turbulence, and turbulence produced at the blade boundary layer (trailing edge vortices). In a comparison of the various potential sources of sound from turbine operation, these two are considered to be the highest contributors, with inflow turbulence interaction dominant at low frequency and trailing edge dominant at high frequency (*Lloyd et al.*, 2011). The model predicts noise levels in the range of 120 dB re μPa below 1000 Hz for inflow turbulence noise and 40 dB re μPa at 100 Hz to 10 kHz for trailing edge noise.

At several existing or planned tidal energy test sites or development areas, noise measurements have been collected to characterize ambient conditions and to quantify sound associated with installation or operation of the turbine. While many of the device-specific data are not publicly available, released results shows a diverse range in measured sound levels and a variety of conclusions on turbine noise propagation in specific environments. A review of 29 tidal and wave energy noise studies was conducted by *Robinson and Lepper*

(2013), and results related to turbine operational noise were available for 7 sites with large-scale TEC devices ($\sim$ 1 MW), located primarily in Europe. As identified by the authors of the review, the studies did not employ consistent units of measurement or consistent methodologies, and variations among factors such as depth and measurement range from the device, data collection methodologies, and physical environmental conditions hinder the ability to make comparisons between locations. However, the findings do show that turbine operation can create sound at levels above marine mammal hearing thresholds, with one particular study (the MCT turbine at Lynmouth) reporting a broadband "effective radiated noise level" of 166 dB re 1 μPa at 1 m; measurements at a range of 250 m indicated that noise levels across a frequency range of 300 Hz to 10 kHz were 10-15 dB re μPa higher during operation when compared to levels when the turbine was not operating (*Robinson and Lepper*, 2013).

A recent study of the sound emitted by a small-scale (10 kW, "community-scale power") cross-flow helical turbine found a strong tonal source with fundamental frequency of around 100 Hz during the optimal operation state, with frequency increasing as rotation rate increases (*Polagye and Murphy*, 2015). Based on the device design, it was suggested that this source is related to generator sound; non-tonal sounds were also recorded, with the suggested source being the interaction of inflow turbulence with the device blades.

These results highlight both the variability and potential intensity of turbine noise, further emphasizing the need to understand existing soundscape conditions prior to installation and to conduct detailed evaluation of device-specific noise.

2.2.3 Pseudonoise (flow noise)

A hydrophone in a high Reynolds number flow can be subject to "pseudonoise" (or pseudosound), a term introduced by Lighthill to describe the pressure fluctuations recorded as turbulent eddies pass across the hydrophone element (*Lighthill*, 1962); this is also referred to as turbulence noise or flow noise in other literature. Pseudonoise pressures are not a true sound signal, as they are not propagating at the speed of sound but instead are convected with the flow. In a turbulent flow, this artificial signal is expected to dominate over the other forms of self noise, which may include electronic noise, caused by preamplifier electrical noise or excess current noise (Jay Abel, personal communication), thermal noise, a high frequency noise caused by motions of molecules in the fluid (*Urick*, 1983), or a second form of flow noise, that which results from turbulence generated in the

wake of the hydrophone (*Strasberg*, 1979). In other flow environments, however, these forms can be significant; recent modeling results suggest that high-speed laminar flows (3-4 m/s) interacting with a hydrophone could produce sufficient turbulent kinetic energy to generate high levels of acoustic power in the immediate wake (*Bharath et al.*, 2015). It is therefore important to identify pseudonoise and apply clear terminology to distinguish artificial and real sound signals.

2.2.3.1 Bandwidth

In the study of SGN by Bassett et al., the effect of pseudonoise was considered to be negligible in the frequency bands of interest (*Bassett et al.*, 2013). The authors used an equation presented by *Strasberg* (1979) that relates pseudonoise frequency to flow speed and turbulence,

$$f = |U|\eta_0^{-1} \tag{2.2}$$

where $|U|$ is mean flow and η_0 is the Kolmogorov microscale, the minimum scale of turbulence, below which viscosity suppresses turbulent fluctuations. When applied to the specific flow characteristics in the study (near bed currents of $\sim$2 m/s and microscales of 0.2 mm, from *Thomson et al.* (2012)), this resulted in a theoretical upper limit of 10 kHz. The authors argue that due to the relative sizes of the microscales and hydrophone receiver, pseudonoise at the higher frequencies would be reduced due to partial cancellation of smaller scale fluctuations as the pressure undergoes phase changes across the hydrophone element; this then results in a reduced measurable upper limit, after which pseudonoise would be below ambient levels. The degree of reduction is difficult to quantify, but generally, highest levels of pseudonoise are produced by microscales greater than twice the largest hydrophone dimension, L, corresponding to a frequency limit above which SPLs may be decreased by partial cancellation (*Strasberg*, 1979):

$$L\eta_0^{-1} \leq \frac{1}{2} \tag{2.3a}$$

$$f < \frac{1}{2}|U|L^{-1} \tag{2.3b}$$

The SPL associated with these fluctuations can also be predicted based on particular flow characteristics: $S_p(f) = 2\pi\rho^2 U_0 S_u(k_1)$, where U_0 is the relative mean current, $S_u(k_1)$ is the one dimensional spectral density of the velocity fluctuations in the direction of the mean current, k_1 is the wavenumber of velocity fluctuations, and $S_p(f)$ is the estimated

spectral density of pressure fluctuations (*Strasberg*, 1979). A number of assumptions are made in the derivation of this relation, including: turbulence is frozen as it passes the hydrophone, pressure caused by fluctuations in other directions is negligible, and the hydrophone surface is uniformly sensitive to pressure. While the validity of these assumptions may not hold in all cases, particularly in relation to the instrument dimensions and materials, the equation does provide a general estimate of spectral densities that can then be converted to SPLs. As would be expected, this relation shows increasing SPLs with increasing flow speed and increasing energy in velocity fluctuations. In accordance with the Kolmogorov microscale, which has shown the turbulence energy spectrum to cascade with increasing k, the highest potential SPLs exist at lowest frequencies.

It is also important to note that these equations are related to the mean relative flow. If the hydrophone is in motion (such as in a drifting configuration), there is still a possibility of pseudonoise where surface currents, which govern the motion of the hydrophone, are different from the water column currents, which govern the flow of turbulent fluctuations. It is therefore important to account for the possibility of pseudonoise even where velocity is reduced by using drifting hydrophone methodology.

2.3 Biophony

A tidal channel can provide a rich habitat for many forms of marine life, which in turn introduce sounds produced by organisms, e.g. vocalizations, echolocation, and physical movement (foraging, migration, etc.). The resulting biophony is therefore a compilation of sounds from different taxa and species, with a range of source levels and characteristics.

Sounds produced by fish can provide an important contribution to the soundscape, particularly where large numbers of acoustically active fish are present; rather than discrete vocalizations, these sounds are often identified as "fish choruses" and can occur over a range of frequencies, from a few hundred Hz to several kHz (*Au and Hastings*, 2008). The research presented in this thesis will focus on the marine mammal contribution to local biophony. The term "vocalization" will be used in reference to sounds produced by mammals; this term is intended for categorical, as opposed to causal, reference, and is used to differentiate sounds produced directly by an animal from those produced by the movement of animals (e.g. splash sounds).

The bandwidth associated with biophony from observed marine mammals in the region

near Grand Passage is presented in table 3.1 (chapter 3); the overall frequency range is between 10 Hz and 150 kHz for the most commonly observed species, indicating a wide bandwidth of possible vocalizations in the soundscape. Mammals produce sound at higher SPLs compared to fish (*Au and Hastings*, 2008), and individual mammals thus have a proportionally higher contribution to the soundscape. Each sound can span a range of frequencies and can have varying characteristics including duration, level, or repetition; each species is capable of producing various signals for different functions. For example, the North Atlantic Right Whale produces sounds characterized as scream calls, gunshots, blows, upcalls, downcalls, and warbles, and observations have categorized corresponding behaviours including contact calls, social interactions, or mating; calls can also be gender- or age-specific (*Parks and Tyack*, 2005). These complexities make acoustical monitoring of marine mammal behaviour a challenging process, which is further complicated by other noise signals in the environment.

The biological response to anthropogenic soundscape changes is uncertain, and is difficult to quantify. A recent study based on passive acoustic monitoring of North Atlantic Right Whales found significant changes in vocalization characteristics that corresponded with increased low frequency ambient noise (*Parks et al.*, 2007); long term comparisons showed an increased start frequency for representative upsweep calls between 1956 and 2000, off the coast of the Northeastern United States, and short term measurements in the Bay of Fundy showed higher start frequencies at higher vessel noise levels. While these observations are non-conclusive with respect to causality of the vocalization changes, the correlation suggests a relation between call frequency and noise level that has implications for anthropogenic marine activities in marine mammal habitats.

2.4 Geophony

2.4.1 Sediment-Generated Noise

Mobile sediment grains generate sound through rigid body radiation from interparticle collisions, and the cumulative effect of a broad grain size distribution and varying collision rates and speeds results in a broadband SGN signature. The expected frequency range of the SGN contribution is based on an empirical relation developed by *Thorne* (1986) for the characteristic peak frequency of the broadband sound spectrum generated from collisions

of equally-sized particles:

$$f \approx 0.182 \left[\frac{E}{\rho_s \left(1 - \sigma^2\right)} \right]^{0.4} \left(\frac{g^{0.1}}{D^{0.9}} \right) \tag{2.4}$$

where E is Young's modulus of elasticity, ρ_s is the density of the sediment grains, σ is Poisson's ratio, g is gravity and D is the grain diameter. While collision sound frequency decreases with grain size, the intensity of sound increases with grain size, yielding a total SGN spectrum that is a function of the grain size distribution within the mobile and immobile sediment fraction.

If a mobile particle collides with a stationary particle, sound will be produced. The mobility of unconsolidated seabed sediments is governed by the bottom stresses generated from boundary layer currents and can be represented by the friction velocity u_*, which is related to the current speed at height z above the bed by the Law of the Wall,

$$U(z) = \frac{u_*}{\kappa} \ln \frac{z}{z_0} \tag{2.5}$$

where z_0 is the roughness length and $\kappa = 0.4$ is von Karman's constant.

The critical friction velocity u_{*c}, or threshold of sediment motion, can be estimated using the Shields parameter (equation 2.6) developed by *Shields* (1936) and a modified estimate (equation 2.7) presented by *Hammond et al.* (1984).

$$\theta_c = \frac{\tau_0}{(\rho_s - \rho) g D} \tag{2.6}$$

$$u_{*c} = 0.18 D^{0.2} \tag{2.7}$$

where $\tau_0 (= \rho u_*^2)$ is the critical bed shear stress, and ρ is the density of water, u_{*c} is in m/s and D is in m.

As indicated by the above equations, a given u_* will correspond to mobility of a given size of sediment. The value of u_* can be estimated using the relation:

$$u_* = \sqrt{C_d} U_{1\mathrm{m}} \tag{2.8}$$

where C_d is the drag coefficient and $U_{1\mathrm{m}}$ is the speed at 1 m above the bed; in a tidal channel, the speed at 1 m is expected to vary in accordance with the tidal cycle, resulting

in tidal variation in u_*. With each estimate of u_*, the maximum sediment size in motion can be estimated using both the Shields and Hammond methods. From the maximum mobile size estimate, a minimum frequency of collision sound (SGN) for those particular flow conditions can be estimated. By computing these estimates over a tidal cycle, the variability in frequency range of SGN can be predicted.

2.4.2 Rain

Rainfall produces underwater sound through the formation of bubbles at the sea surface following impact from raindrops. Sound waves are generated by the collision of a raindrop with the water surface, through impact and rigid body vibrations, and by the free oscillations of entrained bubbles formed following drop impact (*Franz*, 1959). The impact noise is a broadband, short duration impulse (*Medwin and Beaky*, 1989), while the longer-duration noise produced by the bubbles formed following impact has a resonance frequency inversely proportional to the bubble diameter (*Leighton*, p. 183):

$$f_0 = \frac{1}{2\pi a}\sqrt{\frac{3\gamma P}{\rho} - \frac{2\sigma}{\rho a}} \tag{2.9}$$

where a is the bubble radius, γ is the ratio of specific heats of the bubble gas (=1.4 for air), σ is the surface tension ($\approx 0.062 - 0.072$ N/m for seawater, after *Deane* (2012)), P is the local pressure, and ρ is the density of water. As demonstrated experimentally by Pumphrey et al. (1989), bubble entrainment, and thus bubble sound, does not occur with every drop impact but rather is related to a combination of drop size and impact velocity; the initial impact sound, by contrast, is generated with every drop, with an intensity that increases with velocity and drop size. The combination of factors contributing to a rain noise signature was investigated by *Ma et al.* (2005), who characterized acoustic observations and mechanisms based on rainfall parameters. It was also noted that tiny raindrops ($<$0.8 mm) do not have an observable acoustic signature.

Further to the characteristics presented in table 2.1, it has been found that rainfall noise is significantly influenced by wind speed, particularly for small raindrops; with a drop impact at oblique incidence, bubble formation becomes less likely and thus the resonance signal is diminished (*Medwin et al.*, 1990).

In addition to resonance effects, rain-induced bubbles can affect propagation characteristics under some conditions. Following an acoustically active period, quiescent entrained

Drop size	Diameter (mm)	Acoustic mechanism	Frequency (kHz)
Small	0.8-1.2	No impact sound, many small bubbles	13-25
Medium	1.2-2.0	Weak impact sound, no bubbles	1-30
Large	2.0-3.5	Impact sound, large bubbles	1-35
Very large	>3.5	Loud impact sound, large bubbles	1-50

Table 2.1: Raindrop parameters and acoustic signature. Adapted from *Ma et al.*, 2005

bubbles can act as scatterers; this is generally more relevant in the breaking-wave case, where wave-induced turbulence entrains bubbles and thus extends bubble-scatterer lifetime in the water column (*Deane et al.*, 2013). However, in heavy rainfall, subsurface bubble layer effects have been found to result in decreased sound levels at high frequencies increased attenuation (*Ma et al.*, 2005); this effect is generally observed at frequencies greater than 15 kHz, as the size of bubbles entrained in the subsurface layer are small, and therefore absorb sound at higher frequencies.

2.4.3 Wind and Waves

Noise due to breaking waves is also introduced through the resonance of bubbles formed at the sea surface; while the sound is produced by wave action, it has been shown to relate closely to wind speed (*Ma et al.*, 2005). Similarly to rain noise, the level and frequency range of wind-driven noise is dependent on the size of bubbles entrained, but is observed in the range 1-50 kHz, with a negatively sloping spectrum. For wind speeds up to 14 m/s, this slope has been empirically estimated at -5 dB/octave, or $f^{-5/3}$, which aligns with the original sea-state dependent spectra reported by Wenz (*Medwin and Beaky*, 1989).

The bubble plume injected by a breaking wave can have both acoustically active and "quiescent" components, terminology that is used to distinguish the period of bubble formation within a wave (and thus release of acoustic energy from newly created bubbles) and the period of bubble plume evolution (degassing, advection, diffusion) (*Deane and Stokes*, 2002). In the active phase, bubbles introduce sound through resonance, as described in section 2.4.2. Quiescent bubbles can be entrained in the water column by wave-driven turbulence, resulting in a higher concentration of potential scatterers. In a study by *Deane and Stokes* (2002), it was found that the size distribution of entrained bubbles varies significantly with time following a wave breaking event, where the concentration of large bubbles decreases more rapidly due to fragmentation.

The distribution, $N(a)$, of bubble sizes within a plume has been researched in both field

Type	Description	Acoustic signature	Suggested mechanism
A1	Damped, spherical bubble	Constant frequency, damping agrees with theoretical	Shock-excited, spherical bubble
A2	Doubly damped, spherical bubble	Constant frequency, initial damping twice theoretical	As above with additional damping by non-linear dissipation processes
B	Damped with spin-off	Similar to A, with high-frequency component	Unstable larger bubble, shedding smaller bubbles
C	Near-surface, moving bubbles	Amplitude increases then decreases, with change to lower frequency	Increase in dipole strength, followed by shape change and damping
D	Amplitude-modulated	Pressure amplitude modulates with periodicity $<<$ resonance frequency	Interference of resonance from bubbles formed by fragmentation

Table 2.2: Bubble types and acoustic characteristics, adapted from results of *Medwin and Beaky* (1989). Type A (A1/A2) bubbles were most common, occurring during 65% of the 2000 observations.

and laboratory settings, resulting in two distinctive scales separated at a radius known as the Hinze scale: $N \propto a^{-3/2}$ for $a < a_{Hinze}$ and $N \propto a^{-10/3}$ for $a > a_{Hinze}$, where the value of a_{Hinze} is related to the dissipation rate ϵ within the wave-driven turbulence (reported values of $a_{Hinze} \approx 1$ mm). The existence of these scales highlights both the higher concentration of small bubbles and the broad distribution of bubble sizes, both of which can affect the frequency dependence of local transmission losses. The scattering cross-section of a gas-filled sphere peaks at $ka \cong 0.0136$, at which the incoming plane wave has a frequency equal to the bubble's resonance frequency (*Medwin and Clay*, 1998); therefore, a range of bubble sizes will effectively scatter broadband sound.

The characteristics of acoustic emissions from bubbles produced by wave action have been evaluated experimentally in several studies. Research conducted by *Medwin and Beaky* (1989) categorized these emissions into several types (A1, A2, B, C, D), to distinguish the different mechanisms; the experiments were conducted for bubble populations near the surface, where the bubble source acts as an acoustic dipole (i.e. when $kl < 1$, where l is the distance between source and image). Observed damping of the acoustic impulse was compared to theoretical damping based on radiation, viscosity, and thermal conductivity. The results of this characterization are summarized in table 2.2.

As suggested in the description of Type C bubbles, a bubble's distance from a free surface affects its physical and acoustic characteristics. Away from the surface, a bubble is spherical, and resonates at a frequency given by equation 2.9. The authors suggest that bubbles near the surface could have an ellipsoid shape, which results in an increased resonance frequency. As presented in earlier work by *Strasberg* (1953), the frequency

change is proportional to the ellipsoid eccentricity; for example, an eccentricity of 16 (ratio of major to minor axis) results in a proportional frequency increase of 29%. In addition, a spherical bubble at close separation from the surface ("breaker bubbles", those formed at the surface by a breaking wave) will resonate at an increased frequency, via a relation derived by *Strasberg* (1953) based on the electrostatic capacitance of two spheres:

$$f = f_0 \left[1 - \frac{a}{2h} - \left(\frac{a}{2h} \right)^4 \right]^{-1/2} \tag{2.10}$$

where f_0 is given by equation 2.9, a is the bubble radius and h is the depth (with $2h$ being the distance between spheres in the capacitance relation).

The literature reports a wide range of distribution peak size, obtained using various acoustic and optical methods in both field and laboratory settings. In a repeat experiment following the results presented in table 2.2, the bubble size distribution under a spilling breaker in a laboratory was found to peak at 150 μm (*Medwin et al.*, 1990). This size bubble would have a theoretical resonance frequency (f_0) of approximately 22 kHz. With equation 2.10, this would be increased to 33 kHz at a distance $h = a$ from the surface. Another study by *Wu* (1992) reports a peak at around 50 μm radius, which has a natural resonance of 65 kHz and a near-surface resonance of 97.5 kHz at $h = a$. Figure 2.1 shows the frequency change for bubbles of size 150 and 50 μm. The value of h/a where the resonance frequency reaches its natural value is approximately 10; for bubbles of size 50 μm, this occurs at a depth of 0.5 mm. The significance is therefore not in the total change in depth, but rather in the existence of a frequency change in the resonance signature from a single bubble.

In addition to resonance effects following bubble formation, bubbles can introduce acoustic energy through fragmentation due to shear in the surrounding fluid. In contrast to the long history of research on bubble resonance sound (e.g. *Minnaert*, 1933), the fragmentation mechanism has received relatively little attention in the literature. A recent study by *Deane and Stokes* (2008) examined the sound radiated by fragmenting bubbles, finding a wide distribution in peak pressure amplitude. The acoustic signature of an individual fragmentation event was found to exhibit a beat pattern resulting from interference of radiation from the two bubble products, with a combined amplitude that greatly exceeded the original bubble's resonance sound amplitude.

The study also provided insight into the distribution of acoustic energy in bubble pairs

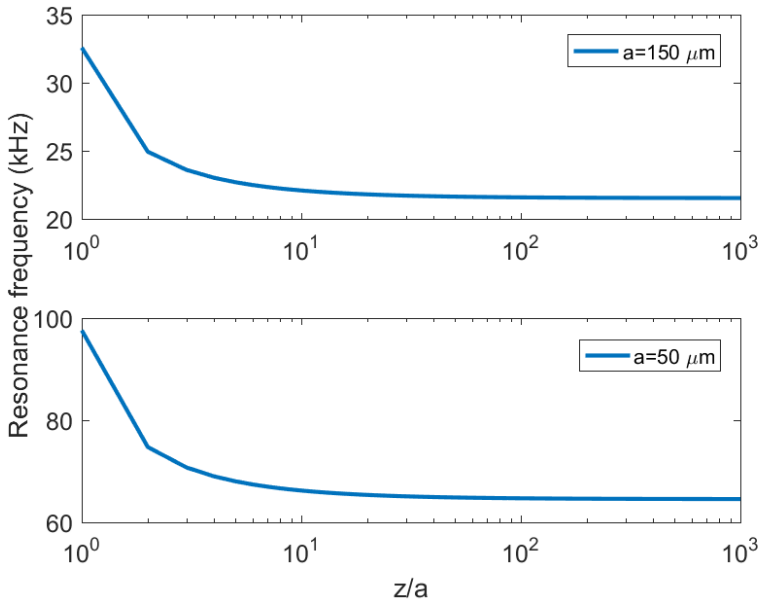

Figure 2.1: Change in resonance frequency near the surface, from equation 2.10 (with z=h). For bubbles of the sizes presented, the change in depth is on the order of 1 mm.

resulting from fragmentation events, showing that energy was equally distributed between bubbles following fragmentation, regardless of bubble size; the researchers postulated that this could be related to the symmetric collapse of the air bridge during the last stage of fragmentation. This suggests that both formed bubbles share an excitation mechanism, implying that all fragmentation products are likely to emit acoustic energy. Fragmentation is therefore an important potential contributor to the noise generated by breaking waves.

CHAPTER 3

INSTRUMENTATION AND METHODS

3.1 Site description

Separating Long Island to the east and Brier Island to the west, Grand Passage (figure 3.1) is characterized by strong currents driven by the large tidal range in the Bay of Fundy. The channel is approximately 4 km long and 1 km wide at its widest point, with depths between 10-30 m and a variable seabed composed of exposed bedrock, gravel/sand, cobbles, and shell fragments. Peter's Island is located near the southern entrance.

Depth-averaged currents in many parts of the channel reach speeds up to 2 m/s, with peak locations exceeding 2.5 m/s (*Hay et al.*, 2013a,b). There is an observed asymmetry in flood (northward) and ebb (southward) current velocity, as well as spatial variability over the channel length; ebb currents are generally stronger, and the highest speeds have been recorded in the southern half of the passage, in the narrow channel between Peter's Island and Long Island.

Surface roughness from wave action in Grand Passage is, on average, minimal, with infrequent occurrence of wind-driven breaking waves; small whitecaps are often observed, but propagating breaking waves do not form under average weather conditions. During storm events, by contrast, significant wave action can develop, with heights up to 2-3 m and 6-7 second periods for winter storms (A. Hay, personal communication). Due to the limited fetch, breaking waves typically form only when the wind and current directions are in opposition; seasonality in wind patterns therefore results in a temporal variation of the tidal dependence of wind-driven breaking waves in the Passage.

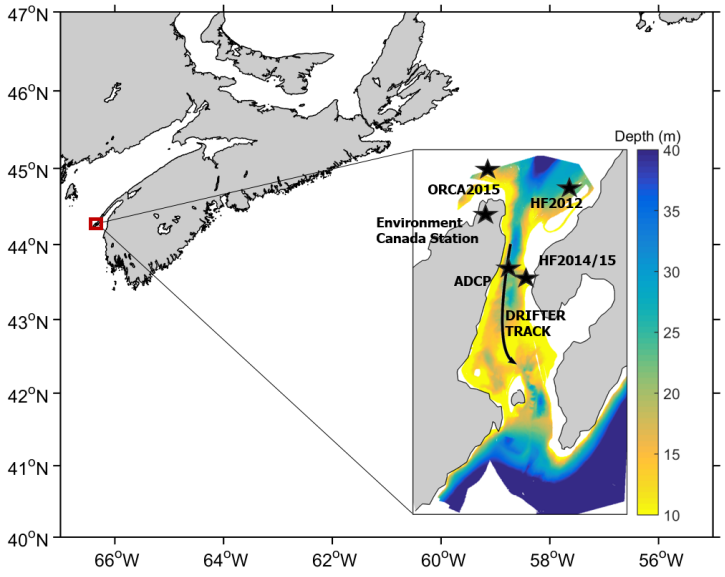

Figure 3.1: Grand Passage is located in Southwest Nova Scotia, near the Grand Manan channel in the Bay of Fundy. The inset shows passage bathymetry and instrument locations, as well as the location of the Environment Canada meteorological station on Brier Island.

3.1.1 Local marine mammals and fishes

The coast of Southwest Nova Scotia is a region of diverse marine life, where the nutrient-rich waters of the Bay of Fundy provide a key habitat for aquatic animals including marine mammals (whales, dolphins, etc.), finfish (sharks), diaromous fishes (striped bass, Atlantic salmon), groundfish (cod, flounder, etc.), pelagics (herring, smelt, etc.), invertebrates (lobster, crabs, etc), and molluscs (mussels, clams, etc.). Many of these animals can contribute to the soundscape; however, the present research focuses on the contribution from marine mammals.

Local marine mammal population data have been compiled based on several years' records (2005-2013) from whale watching cruises as well as a "citizen-science" observation program in 2014-15. The compiled data show an active marine mammal environment at the northern entrance to Grand Passage, extending westward past Brier Island (*Malinka et al.*, 2015a). Within the passage, sightings of larger mammals are infrequent but do occur; the population is typically dominated by harbor porpoise and pinnipeds. Table 3.1 summarizes results pertaining to marine mammal distribution and status in the Grand Passage area (adapted from *Malinka*, 2011 and *Malinka et al.*, 2015a). The "occurrence" refers to the number of sightings during whale tours, which cover a large area, on the order

Class	Species	Occurrence	Species at Risk Status	Vocalization Frequencies (Hz)
Odontocetes	Atlantic white-sided dolphin	Common	None	600-12,000
	White-beaked dolphin	Rare	None	800-325,000
	Harbor Porpoise	Common	Threatened	2000-150,000
	Long-finned Pilot whale	Common	None	100-11,000
	Killer whale	Rare	None	150-25,000
	Sperm whale	Rare	None	100-30,000
Mysticetes	North Atlantic right whale	Common	Endangered	50-2000
	Humpback whale	Common	Special Concern	20-8,200
	Fin whale	Common	Special Concern	10-28,000
	Minke whale	Common	None	60-20,000
	Blue whale	Rare	Endangered	70-950
	Sei whale	Common	Endangered	1,500-3,500
Pinnipeds	Grey Seal	Common	None	0-40,000
	Harbor Seal	Common	None	$<$100-150,000

Table 3.1: Species of regional Marine Mammals, adapted from *Malinka* (2013).

of 500 km^2, to the north and west of Grand Passage.

3.1.2 Human activity

Traffic from small local vessels occurs throughout the year, but is particularly high during summer months due to increased recreational activity, including several whale watch vessels and various private small recreational craft. A number of local fisheries are based in Westport, which results in increased traffic during fishing seasons. A local diesel-electric car ferry crosses the channel approximately twice per hour in the daytime (and as needed during nighttime); the ferry idles dockside between crossings, typically around 35 minutes per hour at the Freeport wharf (Long Is.) and around 5 minutes per hour at the Westport wharf (Brier Is.).

3.2 Data collection

Given the diverse ecosystem in the Bay of Fundy, passive acoustic techniques had previously been investigated as a potential monitoring tool for marine mammals such as the North Atlantic right whale (*Vanderlaan et al.*, 2003); however, the shallow, narrow, high-flow environment in Grand Passage introduces additional constraints in the use of passive acoustic monitoring (PAM). An initial investigation of hydrophone methodologies, specifically targeting pseudonoise reduction, was conducted in 2012 (*Malinka et al.*, 2015b). Results indicated that flowshields of open cell foam on bottom-mounted hydrophones did not result in an unambiguous reduction in pseudonoise levels. Alternatively, drifter-based hydrophone methodology was found to be appropriate for ambient noise characterization.

In the past several years, drifting hydrophones have been successfully used in several high energy sites, in the context of noise emissions from TEC devices (*Bassett et al.*, 2013; *Robinson and Lepper*, 2013). To expand upon the 2012 findings and the successful results at other sites, this methodology was modified to incorporate a drifting hydrophone array that would enable coherent processing and thus support (1) the identification of incoherent pseudonoise effects, (2) improved source characterization, and (3) investigation of second-order noise properties such as vertical coherence.

3.2.1 Moored hydrophones

Passive acoustic datasets were collected via bottom frame moorings over four deployment periods of weeks to months, at the locations indicated in figure 3.1. The instrumentation details and timeframe are provided in table 3.2.

Map ref.	Instrument	Deployment dates	F_s (ksps)	Data type	Storage
HF2012	icListen HF icListen LF	Sept. 6-25, 2012	512 4	FFT & WAV* FFT	On-board
HF2014	icListen HF	Aug. 14-28, 2014	512	FFT & WAV	Cabled to shore
HF2015	icListen HF	Aug. 27-Nov. 22, 2015	512	FFT	On-board
ORCA2015	TR-ORCA	Sept. 15-29, 2015	192	WAV	On-board

Table 3.2: Moored hydrophone deployment details. *Note: WAV files from the 2012 deployment were collected on a 1 minute per hour duty cycle (icListen HF).

The HF2014/2015 location provides long time series data for noise levels within the passage; the frame was moored in a sheltered location, such that pseudonoise effects could

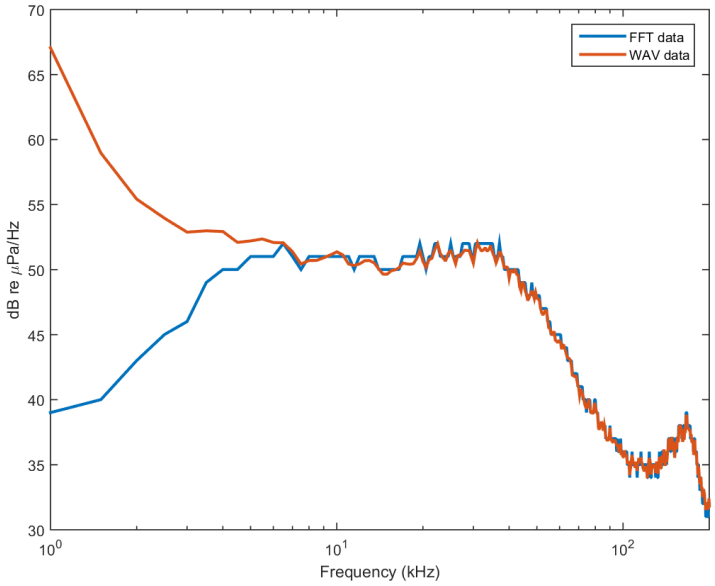

Figure 3.2: Comparison of FFT data with PSD curve computed using the same parameters. The effect of a high-pass filter in the FFT data is evident at frequencies less than 5 kHz.

be minimized. The other moored hydrophone locations were outside the highest flow area, but were still subject to potential pseudonoise.

The icListen HF (Ocean Sonics) is equipped with an onboard digital signal processor that analyses data in real-time, reducing file size and enabling on-board storage of long time series data in "FFT file" format. The files contain processed power spectral levels calculated using specified parameters (1024 points, Hanning window, 50% overlap, 250 segment ensemble average); details on the calculation of FFTs in digital acoustic time series are provided in section 3.3. With the hydrophone set at the maximum sampling rate, this results in power spectral estimates for each 0.25 seconds of data (0.5 seconds for the 2014 deployment), with a frequency resolution of 500 Hz. Prior to computing the energy spectrum, a high-pass filter at approximately 2% of the analog bandwidth is applied to the data to remove the DC offset (A. Guimnan, Ocean Sonics, personal communication). This yields a lower frequency limit of 5 kHz at the maximum sampling rate of the instrument (512 kHz). The effects of the on-board high-pass filter are shown in figure 3.2.

WAV data recorded by the icListen can be stored on the unit's memory card (64 GB) or transfered to external storage in a cabled configuration. WAV files were recorded at 512 kHz during drifting hydrophone data collection, with record length of 1 minute per file. The data were transfered at the completion of each field day to optimize storage capacity,

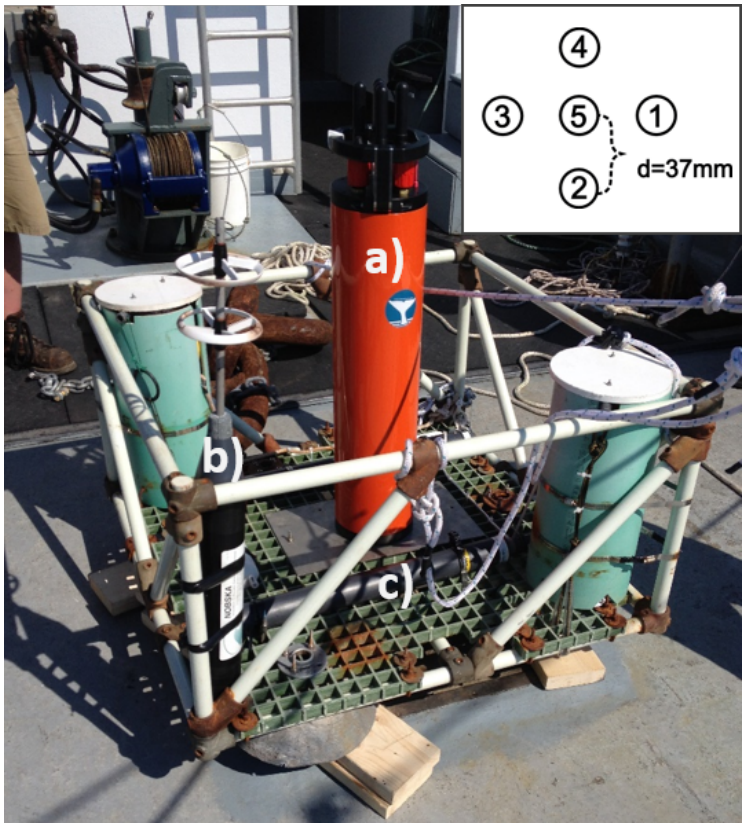

Figure 3.3: ORCA2015 Frame and instrumentation: a) ORCA array and pressure case, b) Nobska MAVS; c) acoustic release; pressure sensor (RBR-Duo) behind MAVS, not visible in photo. Inset: configuration of 5 channels.

enabling storage of both WAV and FFT files on board the hydrophones during drifts.

The 5-channel TR-ORCA hydrophone array (Turbulent Research) has a horizontal configuration with uniform inter-element spacing of 37 mm from center (channel 5) to outside (channels 1-4), as shown in figure 3.3; the configuration results in two orthogonal acoustic axes of length 74 mm across channels 1-3 and 2-4. The instrument housing contains sufficient battery power and storage capacity for continuous-sampling, autonomous deployments of several weeks. The instrument was deployed for a two week period in September 2015, in a bottom-mounted configuration with additional instrumentation to measure flow speeds and hydrostatic pressure (figure 3.3).

3.2.2 Drifting hydrophones

To minimize flow-induced pseudonoise contamination, and to improve the spatial resolution of soundscape characterization, drifter transects were conducted using a vertical array of two synchronized icListen HF hydrophones. The hydrophones were suspended at depths

of approximately 3 and 4.5 m respectively (1.5 m array spacing). The drifter included bungee cables to reduce the vertical motion of the instruments and cylindrical wire brushes (additional drag) to account for the difference in surface flow versus water column flow, thus allowing the drifter to move mainly with the subsurface current.

Transects were completed over 5 days in September 2015, covering several flood and ebb tide periods during both spring and neap conditions; a total of 39 transects were conducted within Grand Passage, with drifter trajectories similar to the sample track provided in figure 3.1. The drifter was deployed and recovered via a rigid hull inflatable boat (RHIB), which drifted with engines off to minimize the vessel noise input during data collection.

3.2.3 Supplementary data

Temperature and salinity profiles (for sound speed) and seabed video were collected from the RHIB during drifter deployments. Additional supplementary measurements and records used in data analysis include ADCP flow speed and backscatter (figure 3.1); diver video; Nobska MAVS flow speed measurements; pressure; meteorological records (hourly wind and 24 hour precipitation); and marine mammal observations. The MAVS was configured to sample at 1 Hz and record data as 10-sample ensemble averages. The ADCP (cabled to shore) sampled at 2 Hz, with 0.5 m range bins.

3.3 Analysis

Analysis of the hydrophone records was conducted in several stages, progressing from visual inspection to quantitative evaluation. The initial stage typically included calculation of PSD from WAV data; generation of broadband, 1-6 hour spectrograms; and visual identification of relevant features (marine mammal vocalizations, vessel noise, sediment noise). Detailed assessment of specific observations was then based on established theoretical and empirical relations as well as concurrent datasets when available.

3.3.1 Spectral analysis

The WAV data were analyzed using spectral analysis techniques to evaluate the soundscape characteristics based on the distribution of acoustic energy in time and frequency. Power spectral densities were calculated using the ensemble-average of multiple overlapping, Hanning-windowed segments (*Oppenheim et al.*, 1999).

The array data were further analyzed to obtain second-order characteristics including phase, cross-spectral density (CSD), and coherency. The CSD between two signals is composed of a real part, the cospectrum, and imaginary part, the quadspectrum, corresponding to the in-phase component and out-of-phase component:

$$S_{xy}(f) = L_{xy}(f) - iQ_{xy}(f) \tag{3.1}$$

The phase, ϕ, is equal to:

$$\phi(f) = \tan^{-1}\left(\frac{\langle -Q_{xy}\rangle}{\langle L_{xy}\rangle}\right) = \phi_y - \phi_x \tag{3.2}$$

The magnitude squared coherency, Γ^2, is defined as:

$$\Gamma^2 = \frac{\langle S_{xy}\rangle^2}{\langle S_{xx}\rangle\langle S_{yy}\rangle} \tag{3.3}$$

The term "squared coherency" will be used in the remainder of this thesis for analyses conducted using the above equation. The term "coherency" will be used in reference to analysis conducted using the coherency function Γ, which has real and imaginary parts. This terminology is adopted after *Jenkins and Watts* (1968, p. 332). The spectral and cross-spectral densities in the relations above are ensemble averages.

3.3.2 Anthropophony

3.3.2.1 Ferry noise

The ferry wharf at Freeport is located within 200 m of the moored hydrophone location (HF2014/2015). This resulted in high ferry noise levels at the receiver when the ferry was located near or at the wharf, during arrival/departure and idling. Given the short range to the hydrophone, noise levels associated with idling or transit could be evaluated over a wide frequency band. Noise levels were calculated from the HF2014 WAV data, using 10 second ensemble averages with a frequency resolution of 10 Hz. To enable assessment of ferry noise without SGN, a departure and transit period during low flow speeds was selected.

3.3.2.2 Pseudonoise

Pseudonoise is generated by non-acoustic turbulent pressure fluctuations passing over the hydrophone element, and is typically present at lower frequencies, with a theoretical

maximum frequency dependent on mean flow speed U and the wavelength of the smallest turbulent spatial scales (Kolmogorov microscales) η_0 (equation 2.2).

With microscales on the order of 0.3 mm (J. McMillan, personal communication) and peak mean currents of approximately 2.5 m/s in Grand Passage, theoretical pseudonoise would extend to 8 kHz. However, the effect of microscale pressures is expected to be reduced by averaging over the surface of the transducer, resulting in an upper limit of observed pseudonoise, above which intensities would decrease (equation 2.3). The instruments used in the present study have a spherical piezoceramic element, and L is thus half the circumference: with a diameter of 1.27 cm (J. Abel, personal communication), the upper limit of frequencies not subject to partial cancellation is 63 Hz. The protective casing around the piezoceramic would introduce additional averaging of the pressure incident on the transducer over a larger length scale (i.e., would increase L). This would act to decrease the upper frequency limit of maximum pseudonoise amplitude.

Turbulence-induced pseudonoise will be at least partially incoherent across a hydrophone array, enabling the identification of pseudonoise via the inter-element squared coherency Γ^2 (equation 3.3). The flow speed dependence can be characterized from co-located flow measurements; this correlation has been conducted using the MAVS flow meter and ORCA acoustic measurements obtained at the ORCA2015 location. The average squared coherency was calculated as the mean of Γ^2 over acoustic axes 2-4 and 1-3, using both 1-minute and 10-second ensemble averages with a frequency resolutions of 1 Hz (192,000-point FFT), and a record length of 1,536,000 samples in each estimate. The band-average squared coherency over $1 < f < 500$ was taken as the geometric mean of Γ^2 for each hydrophone pair (2-4 and 1-3).

The error in squared coherency estimates was calculated using the method described by *Bendat and Piersol* (1986), i.e.:

$$\varepsilon[\Gamma^2_{xy}] = \frac{\sqrt{2}(1-\Gamma^2_{xy})}{\sqrt{\Gamma^2_{xy}}\sqrt{K}} \tag{3.4}$$

where K is the equivalent degrees of freedom. Related confidence intervals were then found as $[(1-2*\varepsilon)\Gamma^2, (1+2*\varepsilon)\Gamma^2]$.

3.3.3 Biophony

3.3.3.1 Marine mammal vocalization bearing

Acoustic measurements from the 5-channel horizontal hydrophone array (TR-ORCA) have been used in the identification of both odontocete and mysticete vocalizations. Low frequency (< 1 kHz) sounds attributed to humpback whales are prevalent throughout the dataset; these relatively narrowband sounds (3 dB bandwidth typically < 200 Hz, see *Stimpert et al.*, 2013), with a duration on the order of seconds, are well suited to bearing determination via beamforming. The bearings of 129 mammal sounds were determined using S_{xy} (equation 3.1), computed for channels 4-2 and 1-3, representing approximately north-south and east-west directions, with 19200-point segments and a record length of 8 segments (0.8 seconds) in each estimate, providing 15 equivalent degrees of freedom. The bearing was then obtained using the two methods described below.

3.3.3.2 Beamforming

The time-synchronized array enables the application of beamforming algorithms, which steer the array beam pattern in azimuth. In this method, the cross-spectral density matrix is weighted by a vector w whose phase is equal to the phase difference between two spatially separated receivers at a given source angle θ. The beamformer output is maximized when the CSD is in-phase with w; i.e., at the value of θ corresponding to the true source angle θ_T. The bearing from each transducer pair has a 180 degree ambiguity. The sign of the phase difference from the orthogonal pair can be used to resolve the ambiguity and obtain results for $0 < \theta < 360°$. The main advantage of beamforming lies in the amplification of signal intensity, improving the ability to resolve source angle where the signal to noise (SNR) ratio is low.

3.3.3.3 Phase difference

In the second method, the source angle θ is calculated directly from the spatial phase difference, $\Delta\phi$, of a plane wave of the form $\exp(\vec{k} \cdot \vec{x} - \omega t)$ arriving at two receivers in a hydrophone pair. Removing the time dependence, this becomes $\phi = \vec{k} \cdot \vec{x}$, which is related to the inter-element spacing d and source angle θ. The advantage of this method is improved computational efficiency, as θ can be calculated directly without the application of a "beam-steering" loop. However, the method is limited to cases where the SNR is sufficiently high. Phase difference analysis has been implemented here only for those low-frequency mammal sounds with relatively high SNR.

3.3.4 Geophony

3.3.4.1 Sediment-Generated Noise

Drag coefficients from a location near the moored ADCP were reported to be 0.0061 and 0.0163 for the flood and ebb tides, respectively (*McMillan et al.*, 2013). In the present research, $U_{1\mathrm{m}}$ was calculated from the law of the wall, using a linear fit based on velocities at 2.11m and 4.11m height above bottom for the period of August 20-29; u_* was then calculated from $u_*^2 = C_{d1\mathrm{m}} U_{1\mathrm{m}}^2$. Histograms of friction velocity with predicted threshold values are presented in figure 3.4. These values indicate that sediment movement is likely for a range of sediment sizes for most of the tidal cycle.

The predicted threshold friction velocities, sediment percent mobility, and associated noise frequencies are presented in table 3.3. Values were computed using the lowest grain size within a sediment class (i.e. $D_{finesand} = 0.125$ mm, etc); percent mobility was based on the assumption that motion of sediments of a particular size would be initiated and maintained for any $u_* > u_{*c}$. The values of u_{*c} are higher using the Shields method, particularly at larger grain sizes. This is expected, as per the results of the Hammond et al. study.

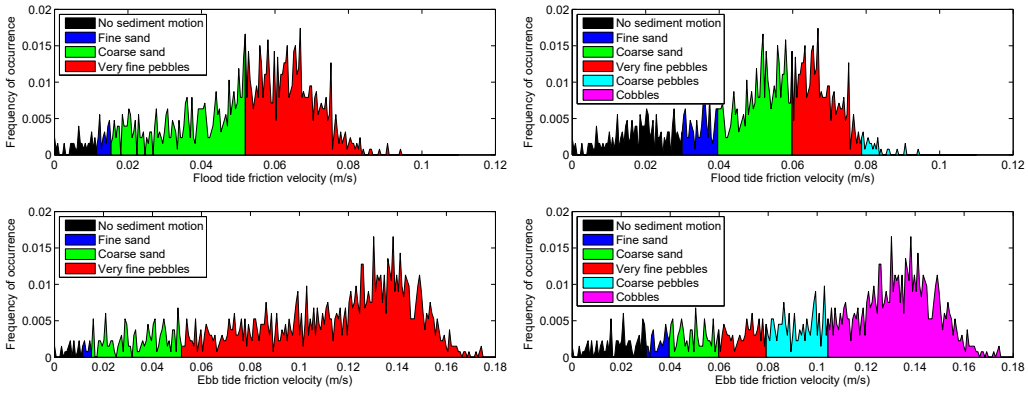

(a) Shields paramter estimate (b) Hammond et al. estimate

Figure 3.4: Estimated friction velocity range and sediment mobility using two methods. The Shields parameter method estimates significantly higher u_{*c} and thus higher mobility for larger sediments.

The ebb/flood asymmetry in predicted mobility suggests a sediment noise regime with distinct flood and ebb tide characteristics. This asymmetry has been evaluated using moored hydrophone records, where time series of the received levels over flood and ebb tides can be directly compared. To ensure that asymmetry results were unaffected by wind

Sediment Type	u_{*c} (m/s)		Mobility: Flood (%)		Mobility: Ebb (%)		Frequency Range (kHz)
	Shields	Hammond	Shields	Hammond	Shields	Hammond	
Fine Sand	0.011	0.03	97	84	99	93	150-1000
Coarse Sand	0.015	0.04	94	75	98	91	40-300
Fine Pebbles	0.052	0.06	56	38	85	83	6-40
Coarse Pebbles	0.11	0.08	0	2	0	74	2-10
Cobbles	0.22	0.1	0	0	0	59	0.5-3

Table 3.3: Predicted sediment motion (portion of tidal cycle for which sediment is mobilized by the flow) and noise levels at the ADCP2014 location

and rain, analysis was conducted for periods where weather conditions were favorable (no rain and low wind).

The predicted mobility rates are based on a seabed composition where unconsolidated sediment of sizes fine sand to gravel exists, which suggests spatial variability in accordance with variability in seabed characteristics. This has been evaluated based on drifting hydrophone results collected over a range of flow conditions. The total SPL over the bandwidth 1-200 kHz was calculated for each drift, and the location of maximum SPL was found using the drifter GPS data. The drift spectrograms were also visually examined, to ensure that the calculated peak SPL aligns with the observed SGN signature during the drift and is not caused by local vessel noise contamination.

3.3.4.2 Rain and wind

Rainfall noise was visually identified in spectrograms based on established characteristics as presented in section 2.4.2. Meteorological records were used to validate the occurrence of rain within a 24 hour period. As no rainfall events occurred during drifter data collection, the rain noise analysis was limited to moored hydrophone records.

A light rainfall event with low winds (< 3 m/s) occurred during the HF2014 deployment, enabling an assessment of rain noise in the absence of wind-driven waves; the total 24 hour rainfall was minimal, at 4.6 mm, but a rain signature is identifiable (figure 4.1c), based on known characteristics of rain sound spectra. The data were high-passed filtered at 1000 Hz, to reduce vessel noise contamination, and were processed with a frequency resolution of 250 Hz. Sample 10-second spectrograms were visually examined to ensure vessel noise was not prevalent in the sample, and a 10-second average PSD was calculated for comparison to rainfall noise spectra.

Significant rainfall with high wind was recorded on several occasions during the HF2015 deployment. These storm events were analyzed using 1-second averages as well as longer

averages (10 minutes), each with a frequency resolution of 500 Hz (as computed in pre-processed FFT files); this enabled a comparison of changes in acoustic features over different timescales, to identify any signficant short-timescale variability in storm effects. With a lower frequency limit of 5 kHz in the data due to a high-pass filter in the onboard processor, the analysis was limited to high-frequency effects.

The acoustic features associated with wind-driven waves were evaluated against hourly wind speed and direction data as well as ADCP backscatter records; analysis focused on high-wind events, where effects are more pronounced. In the available datasets, sustained high wind events ($>$ 10 m/s for several hours) were only observed during the HF2015 recording period.

Plots of 10-minute average spectra in 48 hour periods, corresponding to wind increase and decrease, were generated such that spectra from low and high winds could be directly compared. The difference in SPL between high and low wind was quantitatively evaluated over the course of the storm. Variability in soundscape features attributed to environmental forcing was evaluated against established characteristics as presented in section 2.4.3.

3.3.4.3 Vertical coherence

Results from drifting transects can be used to show both vertical source angle (discrete/tonal sources) and vertical coherence (broadband semi-continuous sources), both of which provide insight into symmetric properties of the noise field. With a wide-aperture linear array of n hydrophones, where $n \geq 2$, a directional density function $F(\theta)$ can be calculated that represents the relative weighting of source components over $0 < \theta < 2\pi$; however, small n can introduce limitations in an accurate calculation of $F(\theta)$. To enable examination of directional symmetry using a pair of hydrophones, *Deane et al.* (1997) present an alternative technique suitable for shallow-water, quasi-homogeneous noise fields, based on a coherency function defined by the directional density function as follows (*Cox*, 1973):

$$\Gamma_{12}(kd) = \frac{1}{2}\int_0^{\pi} F(\theta)\text{exp}(-ikd\text{cos}\theta)\text{sin}\theta d\theta \tag{3.5}$$

where d is the distance between hydrophones 1 and 2, and $k = \omega/c$.

Under quasi-homogeneous conditions, where Γ_{12} is nearly independent of the vertical position of the array (i.e., away from the boundaries), the coherency is related to the finite Fourier transform of a plane wave weighted by $F(\theta)$. Inversely, if the coherency

is calculated from the CSD (equation 3.3), the properties of directional density can be qualitatively inferred from the real (symmetric) and imaginary (asymmetric) components of $\Gamma_{12}(kd)$; a noise field that is symmetric about the horizontal can be distinguished by an $\Im(\Gamma_{12})$ that has relatively small oscillations about zero, as compared to an asymmetric noise field (*Deane et al.*, 1997). In addition, a symmetric noise field can be identified through the relative magnitudes of the real and imaginary parts, where $\Im(\Gamma_{12})$ is low compared to $\Re(\Gamma_{12})$.

If there exist multiple source mechanisms introducing semi-continuous sounds, the coherency properties will be affected by the relative influence of these mechanisms over different frequency bands. During the times that drifting transects were conducted, multiple source mechanisms were present including local vessel traffic, long-range shipping, SGN, and surface agitation. To apply the technique outlined above, record periods with minimal vessel noise have been selected, with the intent of characterizing the varying vertical coherence as a function of seabed composition and flow conditions, via examination of spatial and temporal variation in Γ_{12}.

Equation 3.5 holds for a noise field that can be considered as a superposition of plane waves with orientation $F(\theta)$; this assumes that the field is horizontally homogeneous. In a drifting configuration, the applicability of this assumption is hindered by the constantly changing horizontal position of the sensors. Therefore, the coherency has been calculated using short time frames, such that the effect of changing position can be minimized; 5-second ensemble averages of 0.1 second segments were used in coherency computations.

The coherency function is expected to vary spatially and temporally as the nature of the seabed as a sound source and acoustic boundary changes: spatially, the reflectivity and attenuation properties of the seabed boundary vary as the geological characteristics vary; and temporally, the sound source properties vary as bedload motion, and thus SGN, is initiated by current forcing.

CHAPTER 4

RESULTS: THE SOUNDSCAPE

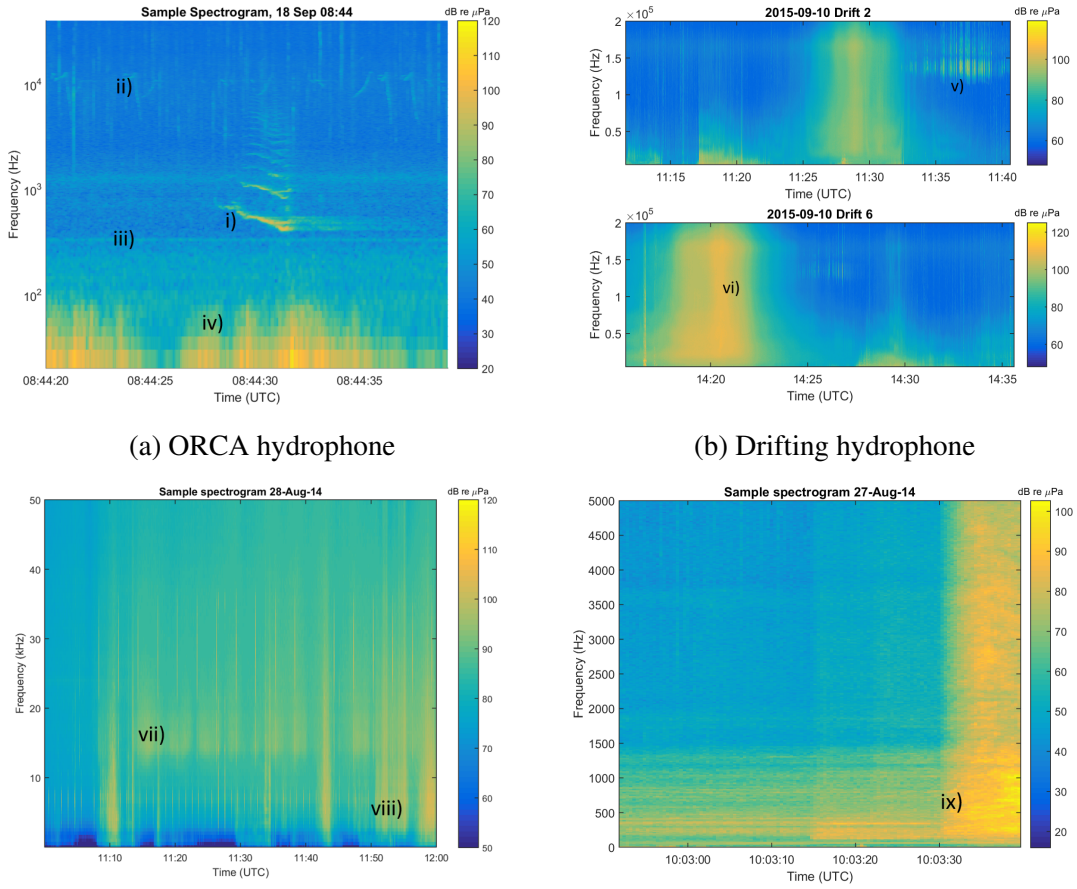

(a) ORCA hydrophone

(b) Drifting hydrophone

(c) HF2014 (moored)

(d) HF2014 (moored)

Figure 4.1: Sample spectrograms from deployments as indicated. Identified signals: i) humpback whale; ii) Atlantic white-sided dolphin; iii) Vessel (rotating machinery); iv) Pseudonoise; v) Harbour porpoise; vi) SGN; vii) & viii) Rain; ix) Ferry departing Freeport wharf.

Visual inspection has provided a qualitative assessment of the soundscape both within Grand Passage and in the coastal region north of the passage. Figure 4.1 provides a sample of visually-identified signals, based on known source and sound characteristics. Results are presented in the following sections.

4.1 Anthropophony

4.1.1 Vessel noise

Moored hydrophones were subject to frequent broadband, intense noise from vessels passing near the hydrophone. Visual inspection of datasets has therefore been used to minimize the contamination of results based on band- or time-averaging. The local ferry is a dominant source of vessel noise, with detectable band-average sound up to the 128 kHz band (see figure 4.9). In addition, high noise levels are generated from several whale-watching boats (outboard and inboard motors) that travel through the passage daily during the summer season, as well as 10-20m fishing vessels and small recreational craft.

A typical ferry noise signature, recorded on a summer day with moderate winds, is presented in figure 4.2. The hydrophone was located approximately 200 m from the Freeport wharf. As indicated in figure 4.2, the ferry generates highest noise levels when departing from the wharf; as the distance between vessel and hydrophone increases (ferry moving toward opposite shore), the noise levels decrease, as expected. Noise from engine idling is also detectable, with a peak at 60 Hz, likely due to machinery rotating at the electrical mains frequency of 60 Hz. The second peak in idling noise at 180 Hz suggests a third harmonic of the 60 Hz signal. Above 180 Hz, the idling signature shows elevated noise levels over frequencies up to 1000 Hz. Idling noise is approximately 10 dB higher when the vessel idles at the Freeport wharf. During transit, the 60 Hz peak is also observed, and the combined broadband noise due to machinery dominates the signal above 100 Hz.

Long distance shipping noise, which is typically observed at low frequencies (*Wenz*, 1962), is not detectable in Grand Passage, despite traffic in the outer Bay of Fundy. At the northern channel entrance, both local, broadband and long-range, narrowband vessel noise (as shown in figure 4.1a) has been measured at the ORCA mooring. The propagation of distant vessel noise into Grand Passage is restricted by the shallow bathymetry in the channel region. In addition, low frequency noise from sources within the passage would likely mask long range shipping noise.

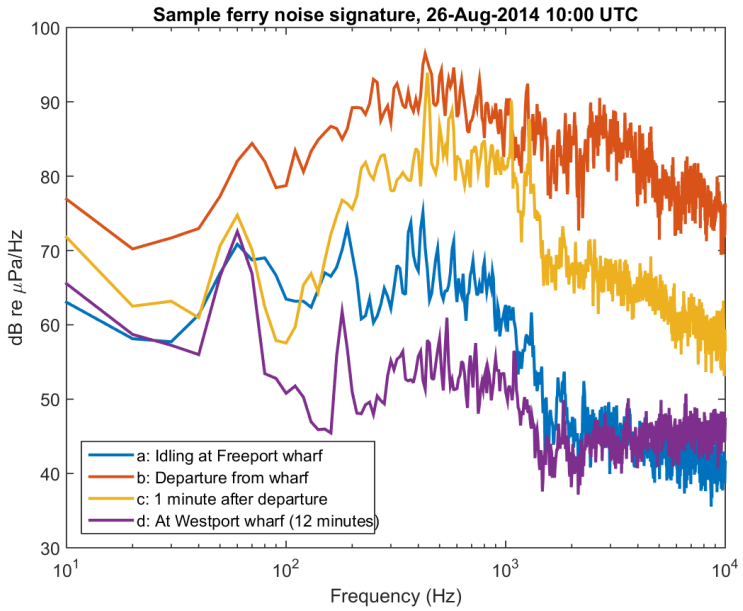

Figure 4.2: Sample ferry noise spectra recorded at HF2014, near the low water mark (minimum flow speed recorded at approximately 09:45). Four PSD curves are presented, showing the difference in noise characteristics during the stages of ferry crossing. Idling noise is dominated by the electrical component signature at 60 Hz (related to diesel-electric engine and/or generator), while transit noise shows high levels over a broad frequency band. The increased noise in d) above 1000 Hz reflects sediment-generated noise due to increasing currents.

4.1.2 Pseudonoise

The effect of pseudonoise on sound levels and coherence at low frequencies was evaluated for a 2 day period using the TR-ORCA dataset. As shown in figure 4.3a, increased low-frequency (<100 Hz) noise levels exhibit a tidal periodicity and are aligned with decreases in squared coherency (average over acoustic axes 2-4 and 1-3). The squared coherency records show variability over a wider frequency range, with $\Gamma^2 < 0.3$ observed at frequencies > 200 Hz. The difference in the effect of pseudonoise on the power spectrum versus the coherency spectrum is likely a result of partial cancellation, whereby pressure fluctuations with a small wavelength relative to the receiver size undergo phase changes as they pass over a receiver surface. The amplitude of pseudonoise at higher frequencies is thus reduced; as was discussed in section 3.3.2.2, an upper limit of pseudonoise amplitude is estimated to occur at $f \approx 63$ Hz, based on the instrumentation used in this research.

However, given the scale of turbulence in a high-energy environment, theoretical pseudonoise extends to several kHz. At this location outside the channel entrance (with lower flow rates), the dissipation rate and microscale dimension are not known, but it is estimated that pseudonoise effects could still extend to several hundred Hz; based on turbulence characterization within Grand Passage, the upper limit in the highest flows is estimated to be 8 kHz (see section 3.3.2.2). Even with a lower recorded amplitude above $f = 63$ Hz due to partial cancellation, the characteristics of pressure from turbulent fluctuations are unique to each receiver for the full range of turbulence scales, resulting in incoherent recordings over a wide bandwidth. The frequency range for which low squared coherency values are observed is therefore much higher than the frequency range for which flow-induced elevated PSD levels are observed.

To directly assess the relationship between pseudonoise and flow, the average value of Γ^2 in the band $0< f < 500$ Hz was used as a proxy for the existence of pseudonoise, and was compared to local flow speed measurements. The highest average inter-channel squared coherency (average between channels 1-3 Γ^2 and 2-4 Γ^2) is observed during low flow periods, as shown in figure 4.3b, with values decreasing significantly with increasing flow speed. The variation in coherency is strongly aligned with local flow changes, on long time scales (on the order of hours). This has implications for monitoring of low-frequency marine mammal sounds, such as those produced by fin or minke whales, as pseudonoise masking becomes increasingly probable at higher flow speeds.

An examination of pseudonoise and flow speed on shorter time scales (periods of 5 minutes) found that correlation over $\mathcal{O}(1)$ minute windows is weak; this could be due to flow orientation effects, where the instrumentation could be disrupting the local flow regime and thus the flow conditions at the hydrophone could be much different than those at the MAVS.

4.2 Biophony

Within Grand Passage, harbor porpoise sounds are significantly more common than any other detected mammal sound. Outside the passage, where noise contamination from vessel traffic is lower, cetacean sounds at sub-kHz frequencies have been detected: in the September 2012 record, this included right whales and humpback whales, and in the 2015 record, humpback and minke whales. No right whale sounds were detected in 2015,

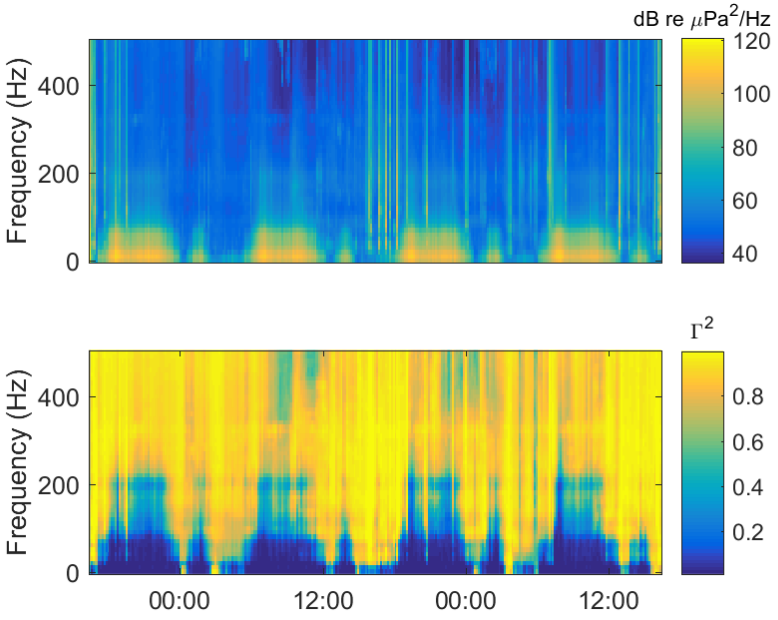

(a)

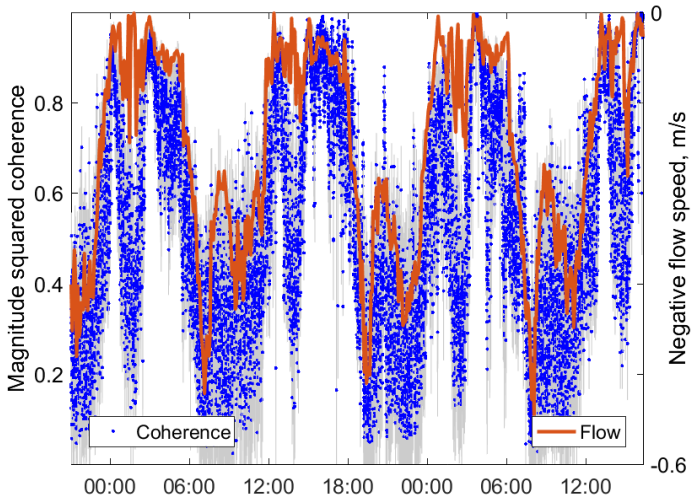

(b)

Figure 4.3: 2 day time series of (a), 10-second average PSD and squared coherency from TR-ORCA array measurements and (b), band-average squared coherency over $0< f < 500$ Hz and local flow speeds. The correlation between increased noise levels and low Γ^2, particularly below 100 Hz, has a tidal periodicity. The effect of pseudnoise on coherency extends to $\sim$200 Hz, whereas noise effects are most significant below 75 Hz, likely due to partial cancellation of turbulent pressure fluctuations over the receiver surface. The shading in (b) indicates 95% confidence interval for Γ^2 estimates. The band-average Γ^2 has an irregular amplitude variation that is strongly correlated with flow speed.

whereas the detection rate for the 2012 period was ~ 0.1 per minute for the 1 minute per hour duty cycle WAV data collection. Right whale numbers in the Bay of Fundy have been anomalously low since 2010, but 2015 sighting numbers were higher than 2012 in this period, with surveys reporting 34 and 10 sightings in August-September of 2012 and 2015, respectively (Kimberley Davies, personal communication). The small numbers of right whales in the Bay of Fundy in recent years is the subject of ongoing research at several institutions.

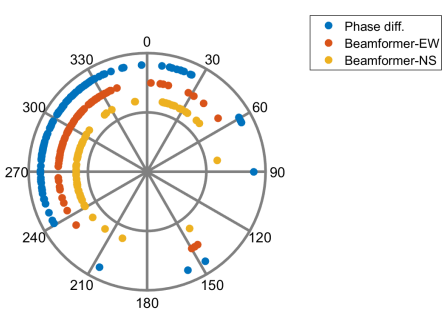

(a) Low frequency mammal sounds source bearing from ORCA2015 location, 17-19 September.

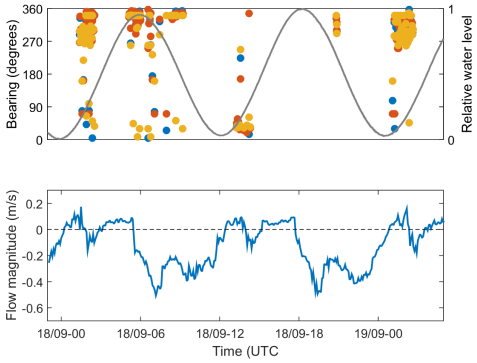

(b) Time series of detections and bearing with water level and flow variation.

Figure 4.4: Distribution of bearing calculated for 129 humpback whale vocalizations. The distribution agrees well with past vessel-based observations of marine mammals in the region (*Malinka et al.*, 2015a).

For each of the 129 identified humpback vocalizations, source bearing was computed using the two methods described in section 3.3. Beamformer-NS values were generated from the approximately north-south acoustic axis between channels 4 and 2, and Beamformer-EW values were generated from the east-west axis between channels 1 and 3. Phase difference values are the mean value of θ calculated from ϕ_{42} and ϕ_{13}. The computed bearings were adjusted for the ORCA's heading and the local magnetic declination of 16.87 degrees.

The distribution of source bearings is broad (figure 4.4), but concentrated mainly in the northwest quadrant: i.e. toward Grand Manan basin and the entrance to the Bay of Fundy, which is where the whales are seen most frequently. Results from the two methods show good agreement, indicating that for the humpback sounds dataset, the computationally efficient phase difference technique is an effective method for bearing analysis.

The detected whale vocalizations are temporally distributed in groups separated by

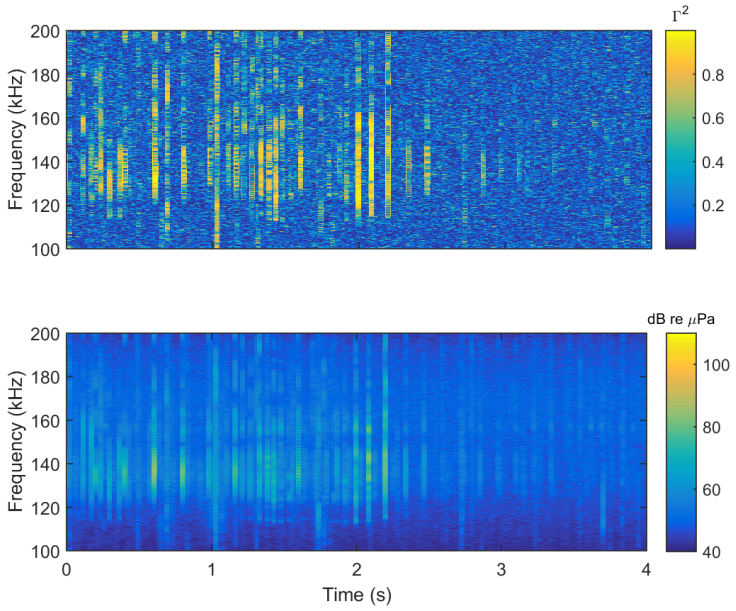

Figure 4.5: Identification of harbor porpoise sounds through squared coherency (upper) and SPL (lower). The porpoise signals have higher Γ^2 than the background noise (primarily SGN), and thus the signal to noise ratio (SNR) is improved in the coherency spectrum.

periods of several hours. To examine this distribution in relation to the tidal cycle, the detections are plotted together with pressure and flow in figure 4.4b. While the record length is short, it is observed that there are two significant groups of detections (approximately 30-40 vocalizations in each group) during both overnight flood tides (near 00:00-03:00 local time). This could be an indication of improved visual signal identification due to reduced masking by broadband local vessel traffic noise. The increased number of detections at high water compared to low water also suggests the possibility of a tidally-dependent whale presence, where the number of whales near the ORCA2015 location is higher at high water.

Harbor porpoise sounds have been identified in the HF2014/2015 moored hydrophone records and 2015 drifting hydrophone records. The drifting vertical array enables examination of second-order characteristics, and it has been found that porpoise noise identification is improved using coherent processing. Spectra from drifter recorders were calculated with a frequency resolution of 100 Hz, 50% overlap, and ensemble averages of 4 segments per estimate. The squared coherency was then calculated from equation 3.3.

A comparison of harbor porpoise vocalizations identified through both intensity and squared coherency is provided in figure 4.5. Figure 4.6 provides a time series of the average

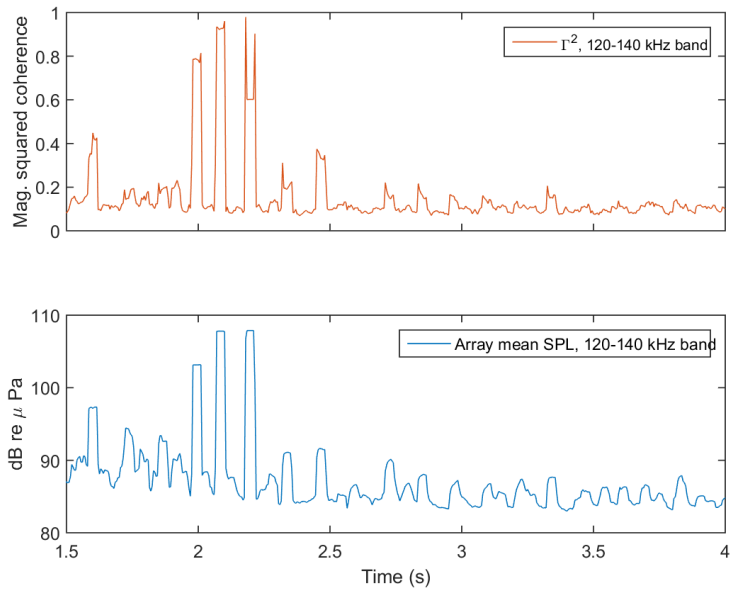

Figure 4.6: Time series of squared coherency (upper) and SPL (lower) for a portion of the record presented in figure 4.5. The SPL was computed from the mean PSD for both hydrophones in the array; band average values were computed as the geometric mean of Γ^2 and SPL, respectively, between 140 and 160 kHz. The SNR was computed from the peak value (at $\sim$ 3 s) and average noise over 4-5 s. SNR_{Γ^2} was found to be 8.9, while SNR_{dB} was found to be 1.3.

Γ^2 and SPL over the frequency band 140-160 kHz. The increase in visual identification using a coherent processing approach is immediately apparent, due to the low coherence of background noise; the band-average signal to noise ratio in Γ^2 is 8.9, compared to 1.3 in dB. The noise field is predominantly SGN over this frequency range (140-160 kHz), which, as a superposition of sound radiated from multiple collisions with a wide variance of source signatures and amplitudes, is relatively non-stationary compared to a sustained deterministic source (harbor porpoise click train). Thus, over the appropriate time window, the porpoise vocalizations are enhanced, while the SGN noise is suppressed in the coherency spectrum.

This finding has implications for detection of marine mammal signals in the passage, particularly at high frequencies where intense SGN can decrease the signal to noise ratio or where propagation is constrained by higher losses as compared to low-frequency mammal signals.

4.3 Geophony

4.3.1 Sediment-Generated Noise

In the northern end of the passage, and diminishing southward as the channel widens, SGN is a dominant source over a wide bandwidth. The drifting hydrophone results (figure 4.1b) show a peak SGN intensity in a region of known "gravel waves", where *Stark et al.* (2013) found seafloor dunes to have wavelengths of 9-14 m and heights of $\sim$0.2-0.4 m, and where diver video shows the sediment to be a loosely compacted mix of gravel/sand/shell hash. Seismic profiles from the Passage suggest a gravel/sand layer thickness of 5-10 m in this region (*CSR*, 2014). The location of maximum SGN (figure 4.7) is consistent over all drifting records, for both flood and ebb tides and in spring and neap conditions.

As shown in figure 4.8, the SGN spectra from the drifting hydrophones differ significantly from the observed open-ocean wind-driven ambient noise slope of $f^{-5/3}$ at frequencies above 1 kHz (*Wenz*, 1962); recorded noise levels are elevated in the 10-100 kHz band, due to the increased generation of acoustic energy by sediment collisions. The figure also shows a consistent difference in intensity recorded by the drifting hydrophones compared to the moored hydrophone, likely due to transmission loss; the location of maximum SGN is approximately 400 m west of the mooring location.

The flood/ebb flow asymmetry results in an asymmetric SGN signature. The recorded

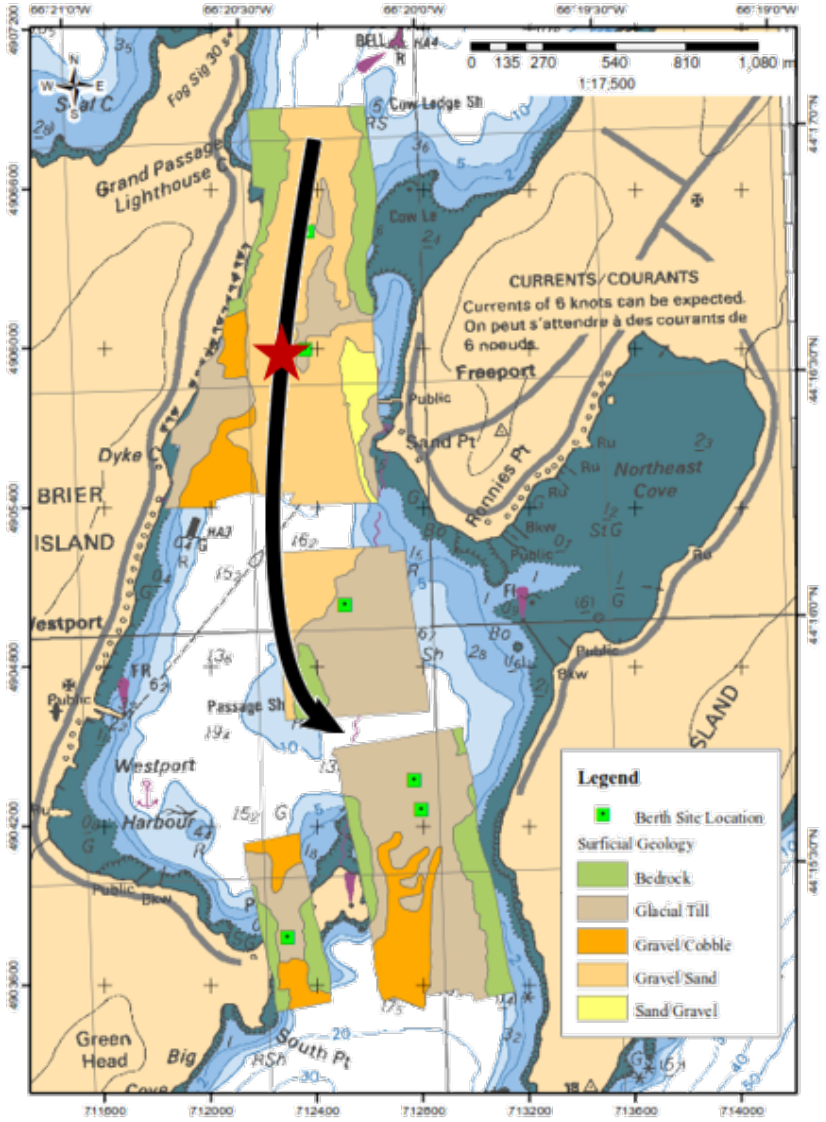

Figure 4.7: Representative ebb tide drifter track (black line) and location of peak SGN intensity (red star). Map adapted from *CSR*, 2014.

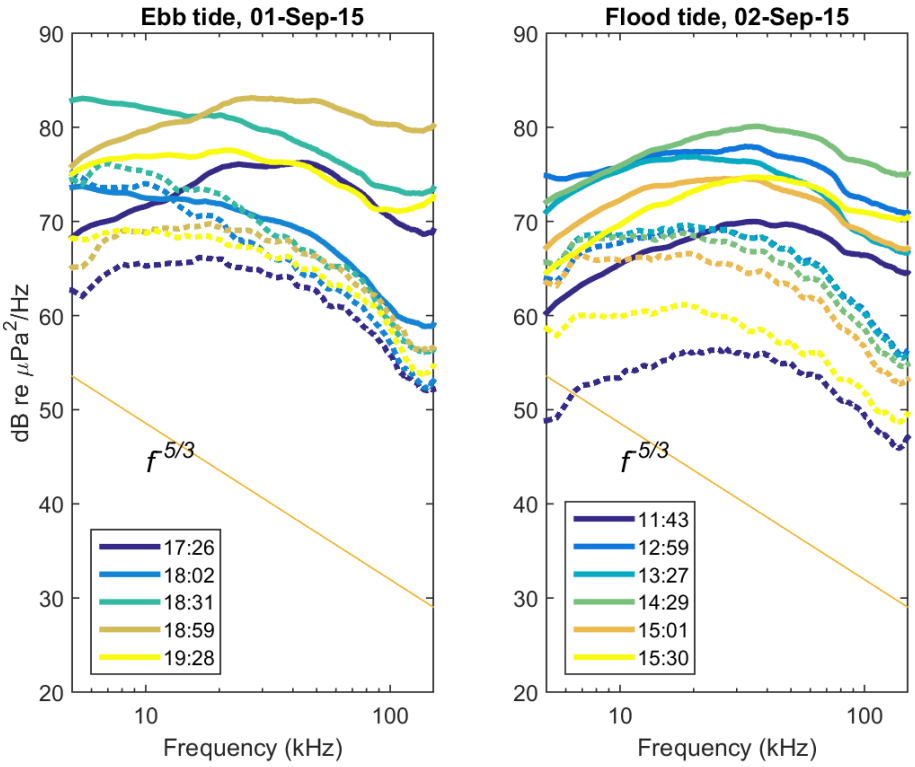

Figure 4.8: Comparison of SGN spectra from ebb and flood tides on two consecutive days, from the peak SGN intensity recorded during each drift; spectra are two-minute ensemble averages from the lower drifting hydrophone (solid lines) and corresponding records at the same time taken at the moored hydrophone (dashed lines). The spectra show a significant deviation from the $f^{-5/3}$ relation. Ebb tide records show increased acoustic energy and a peak at lower frequency compared to flood tide.

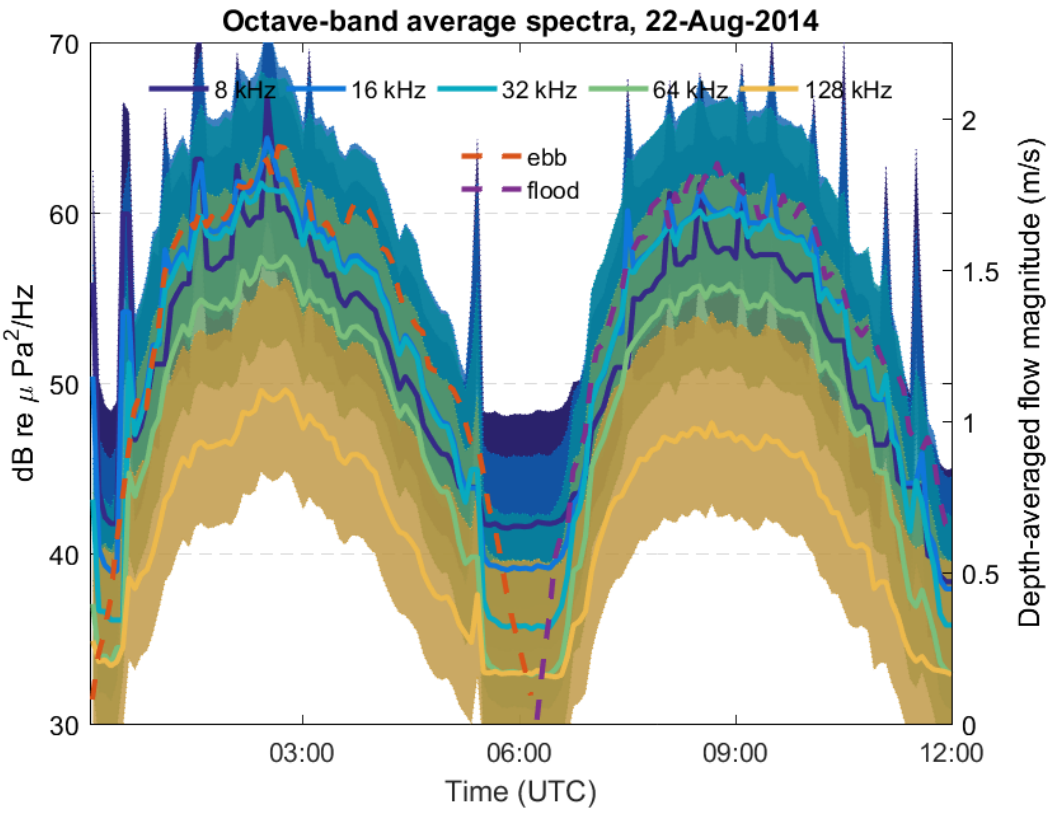

Figure 4.9: Time series of octave-band average SGN over a tidal cycle during neap conditions. Shading indicates 95% confidence interval. Ebb tide shows consistently higher levels, particularly in the 8-32 kHz bands. The observed flow speed peak at 03:00 correlates well with recorded noise levels in all bands. The sporadic noise peaks are caused by the local ferry, running as needed during night hours.

intensities are higher during the ebb tide, particularly for frequencies of $f < 10$ kHz; this agrees with predictions presented in figure 3.4, which suggested a higher fraction of the larger-grained sediments should be mobilized during the ebb. Figure 4.9 shows the band-average SGN over a tidal cycle (neap conditions); flow speeds are depth-averaged, and both flow and noise are 5-minute averages.

There is a strong correlation between noise levels and flow speed, which is particularly pronounced during peak ebb currents near the 03:00 mark. As shown by the dashed lines in figure 4.9, there is an asymmetry in flow speeds, and in flow variability during peak speeds, that is reflected in the sound PSD. In particular, the ebb flows show a distinct peak followed by a steep initial decrease of ~ 0.5 m/s just before 03:00; the sound PSD shows an associated peak and decrease.

During ebb conditions, noise levels are at a maximum over a wide bandwidth (8-32 kHz), whereas flood conditions show a peak in the 32 kHz band. As shown in table 3.3, the higher friction velocity during the ebb tide is predicted to mobilize pebble-size grains for a longer time interval compared to flood (38 and 83 per cent of flood and ebb tides, respectively, based on the Hammond estimate), which would result in increased noise over the 6-40 kHz bandwidth. At higher frequencies, the flood/ebb noise levels are nearly equal, which again agrees with predictions, since high rates of sand grain mobilization are expected during both ebb and flood.

Figure 4.9 also highlights the significance of the SGN contribution. The intensity difference between low flow periods (slack tide) and peak flow is on the order of 20 dB; this is the measured difference at the moored hydrophone location, which is known to be sheltered from the strongest flows.

4.3.2 Vertical coherence

The effect of SGN on the noise field symmetry in the horizontal plane was evaluated using records from a pair of time-synchronized drifting hydrophones with a vertical spacing of 1.5 m, based on the methods presented by *Deane et al.* (1997) (as described in chapter 3). The data were processed with a segment length of 0.1 s, resulting in a frequency resolution of 10 Hz; the segments were ensemble-averaged over a period of 10 s. In each 0.1 s segment, the movement of the drifting hydrophone would be minimal, and it has been assumed that the effects of any motion would be negligible. The 10 s acoustic records were taken from a single drift, with a total drift duration of 5 minutes.

The real and imaginary parts of the coherency function (equation 3.5) from peak SGN conditions and no SGN conditions are shown in figures 4.10 and 4.11, respectively. In shallow water, much of the SGN would be reflected by the surface, resulting in sources at the receiver that originate over a wide range of angles in the vertical, exhibiting symmetry in a horizontal plane located away from the surface or bottom. This symmetry appears in the coherency results as relatively low oscillations in the imaginary part, with amplitude of order 0.2 (figure 4.10); these small oscillations are characteristic of a symmetric noise field. The magnitude of the imaginary part is also much lower than that of the real part, again indicating a symmetric noise field. The real coherency decreases at high frequency, likely resulting from the compilation of the many impulsive, low-amplitude sound sources that are generated with each sediment grain collision.

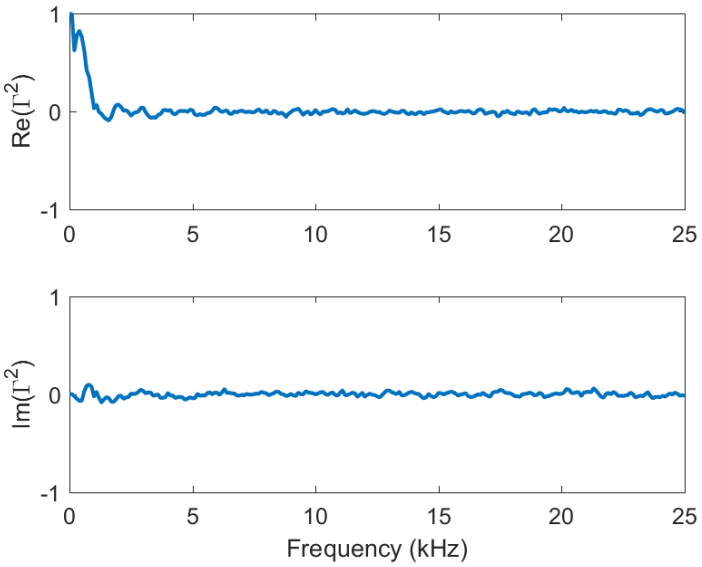

Figure 4.10: 10-second average Γ^2 measured from drifting hydrophone records, during peak SGN conditions. The real coherency is low at high frequency, highlighting the effect of a compilation of many SGN sources received during a 10 second period. The imaginary coherency shows relatively little oscillation about zero, and has a magnitude much lower than the real coherency, indicating a noise field that is symmetric about the horizontal (after *Deane et al.* (1997)).

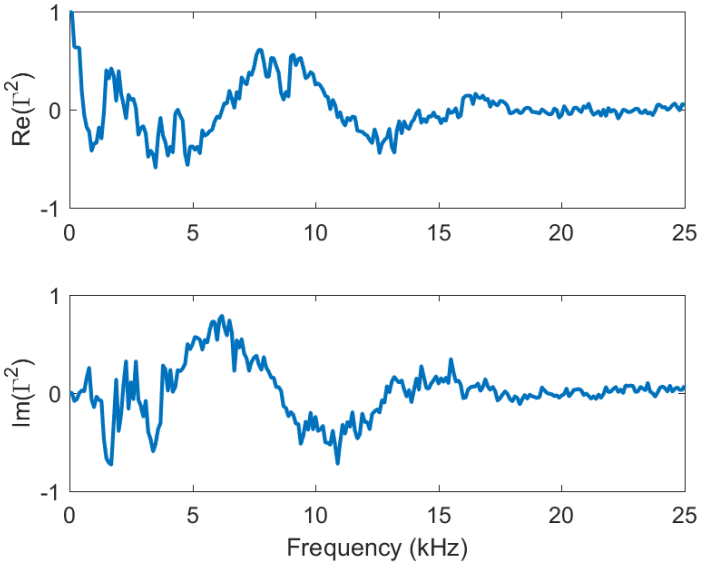

Figure 4.11: 10-second average Γ^2 with a frequency resolution of 100 Hz, computed from drifting hydrophone records, taken from a region where little to no SGN was identified in the recordings ($>$500 m from peak SGN location). In contrast to the high SGN region, the imaginary coherency has significant oscillations about zero, and is nearly equal in magnitude to the real coherency, indicating an asymmetric noise field. In this region, the majority of noise sources are of surface origin (vessels, surface agitation).

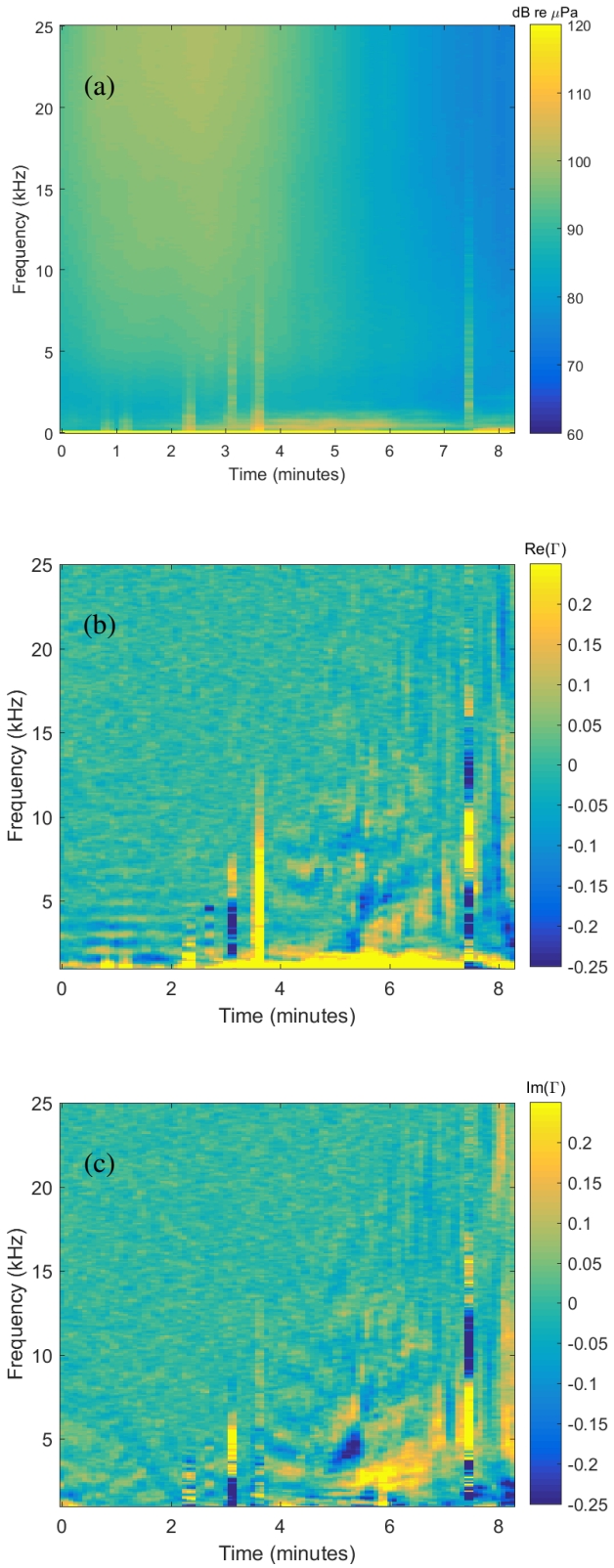

Figure 4.12: SPLs (a) and coherency (b: real part and c: imaginary part) during a single ebb tide drift. The lower frequency (<25 kHz) component of SGN is shown in (a). Low frequency noise (<1 kHz) is coherent over the course of the drift, indicating possible long-range vessel noise. Local vessel noise appears as spikes in the SPLs at the 2-4 and 7.5 minute marks. Away from the peak SGN, the real and imaginary coherency show oscillations over a larger frequency band as compared to the peak SGN location, and show inconsistency in amplitude and period. The transition from consistent coherency patterns above the mobile sediment region to variable coherency patterns away from the SGN region highlights the spatial variability in directionality characteristics in Grand Passage.

The results from a region of no SGN show much larger oscillations in the imaginary part of the coherency, with amplitude of order 1 (figure 4.11), characteristic of an asymmetric noise field. The magnitudes of real and imaginary parts are nearly equal, which again indicates asymmetric properties. Non-SGN noise sources in Grand Passage, such as vessel noise or surface agitation, are largely concentrated near the surface; in addition, the location where this data sample was recorded is known to have significant kelp growth on the bottom, which could act to absorb acoustic energy and thus minimize bottom reflections.

The SPLs and coherency characteristics over a single ebb tide drift are shown in figure 4.12, for $0 < f < 25$ kHz. SGN is observed in the first half of the drift, and the coherency properties show symmetric characteristics for the first $\sim$3 minutes of the drift, i.e. the real part of the coherency function has small oscillations about zero and the imaginary part has a low magnitude. As the hydrophones drift further south and away from the SGN region, the coherency oscillations spread to higher frequency (> 10 kHz) and the real and imaginary parts are nearly equal in magnitude. During most of the drift, low frequency (< 1 kHz) noise has high real coherency, likely indicating long-range vessel noise.

4.3.3 Rain

A rainfall event with light winds occurred during the HF2014 deployment, enabling an assessment of rain noise in the absence of wind waves. The total 24 hour rainfall was 4.6 mm, but a rain signature is identifiable (figure 4.1c), based on the known characteristics of rainfall-generated noise (*Ma et al.*, 2005). The WAV data were high-passed filtered with a 1 kHz cutoff, third-order Butterworth filter, to reduce vessel noise contamination. Sample 10-second, 250 Hz-resolution spectrograms were visually examined to ensure the sample was not contaminated by local vessel noise, and a 10-second average power spectrum was computed for comparison to rainfall noise spectra.

The resulting spectra for the rain event are shown in figure 4.13, indicated by the solid lines. Two rain cases are shown: case 1, recorded at 11:15, and case 2, recorded at 11:52. Also shown are the spectra on the previous day (dashed lines) recorded during the same tidal flow stage (i.e., time-shifted by -50 minutes), which exhibit the characteristic SGN signature. Both rain noise cases deviate significantly from the SGN spectra at frequencies below 30 kHz. Case 1 exhibits both a defined peak at 10.5 kHz and a broadband intensity increase over 5-100 kHz; at the peak, the noise results in a PSD increase of approximately

15 dB, falling to $\sim$ 3 dB at $f > 50$ kHz. This indicates the resonance effect of a given bubble size range created by small raindrops ("type II" bubbles after *Ma et al.*, 2005), which introduce sound at 13-25 kHz, as well as the less significant impact noise generated over a wide frequency band. The previous-day spectra corresponding to case 1 (dark blue dashed line in figure 4.1c) were recorded during flows of $\sim$ 1 m/s (depth-averaged), indicating that SGN intensity would be below its peak value. Comparing case 1 rain spectra to the higher intensity SGN (light blue dashed line), it is evident that this noise would not be distinguishable above peak SGN for $f > 20$ kHz.

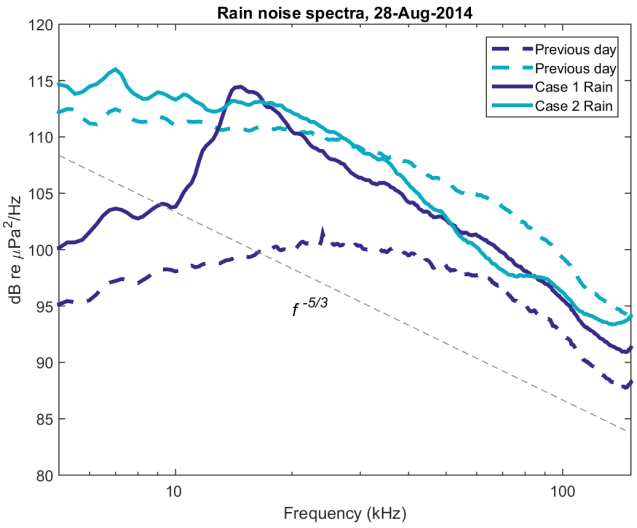

Figure 4.13: 10-second average spectra recorded at HF2014 during a rainfall event with low winds. The cases have been characterized as 1) small raindrop noise, identified by a peak at 14-20 kHz due to small bubble resonance; and 2) heavy rain/large raindrop noise, identified by a broadband increase in intensity and a steep negative slope at $f > 30$ kHz.

Case 2 rain, which occurred during peak flow speeds ($\sim$ 2 m/s), shows a small increase in intensity of approximately 2 dB over the 5-20 kHz band. Above 20 kHz, however, the spectral slope begins a steep decrease ($\sim f^{-3}$), greater than the typical SGN slope as well as the Knudsen wind-driven slope. The lack of a distinctive peak in this case suggests that raindrops were of a medium-large size, resulting in a wider range of potential bubble sizes generating sound over a wider bandwidth; in addition, impact noise is louder for larger drops (see table 2.1), which could further increase sound levels over this frequency range. The steep slope, and decrease in PSD compared to the previous day, indicates attenuation of SGN at high frequencies. This attenuation could be due to the characteristic subsurface bubble layer associated with heavy rainfall (*Ma et al.*, 2005).

CHAPTER 5

RESULTS: STORM EVENTS

The SGN characteristics presented in the previous chapter exhibit significant variability during high-energy weather events. These storm conditions result in a soundscape in which both source and propagation characteristics are modified as compared to "normal" conditions via an increased concentration of bubbles in the water column. The effect of the bubbles is to introduce acoustic energy through resonance, and to attenuate broadband sound through scattering. Based on analyses of broadband noise levels and concurrent records of wind speed and water column acoustic backscatter, the cumulative effect has a strong association with the combined oceanographic/meteorological conditions. A significant storm event on 29 October 2015, with winds speeds of 7-19 m/s and 39 mm of rainfall, has been analyzed to quantify the observed variability and evaluate the relevant mechanisms. A subsequent analysis of the full data record from this location has also been conducted to identify trends in variability features.

5.1 Single storm event

Figure 5.1 shows 10-minute average power spectral density curves from the HF2015 moored hydrophone on 28-29 October, 2015, with one sample PSD curve shown per hour. Based on hourly wind velocity and 24 hour precipitation measured at the nearby Environment Canada weather station (Brier Island), high winds persisted for much of the day, with increasing speed throughout the morning followed by a change in direction and decrease in the afternoon (figure 5.4b). PSD curves from the storm day (solid lines in figure 5.1) are shown from 10:00-18:00, corresponding to wind speeds in the range 8-19 m/s. The dashed lines indicate spectra from the previous day (average wind conditions, no

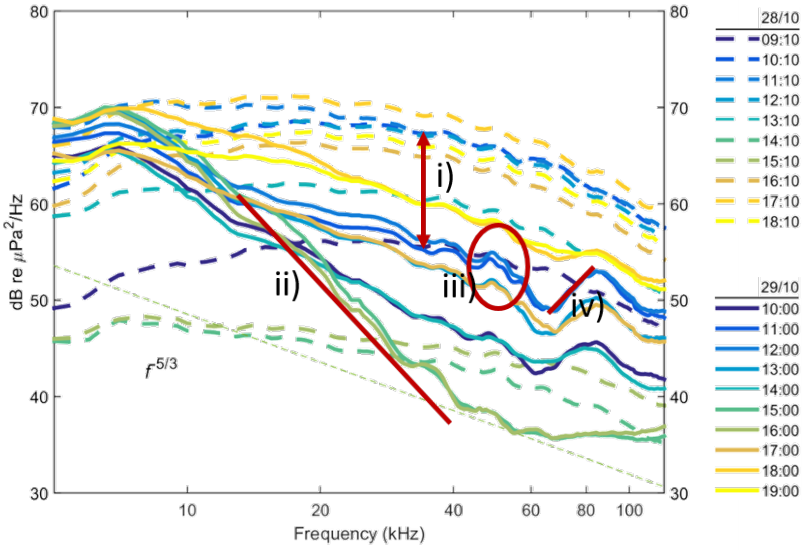

Figure 5.1: 10-minute average PSD from storm day (solid lines) and previous day (dashed lines), recorded at HF2015. Spectra are taken once per hour, with previous day spectra shifted by 50 minutes to represent approximately the same stage in the tidal cycle. The red lines are a visual identification of the features discussed in the following sections.

rain), shifted by 50 minutes to represent approximately the same stage in the tidal cycle; these previous day PSD curves show characteristic SGN, as discussed in section 4.3.1. The storm spectra show significant variation from the characteristic SGN spectra.

Several features of this variability, identified in the figure as i-iv, can be interpreted as follows: (i) the lower noise levels over a broad bandwidth indicate increased attenuation of SGN, caused by a higher concentration of bubble scatterers in the water column, injected by breaking waves; (ii) the steep slope in spectra over two consecutive hours indicate heavy rain, which can form a subsurface bubble layer that attenuates the high frequency component of rain noise (*Ma et al.*, 2005); and (iii) the peak near 50 kHz indicates resonance from small bubbles formed by small raindrops. The fourth feature (iv), a trough and slope between $\sim$ 70-85 kHz, has not been previously reported in the rain and wave noise literature, which has generally been confined to frequencies below 50 kHz.

The difference in PSD levels over the course of the storm has been quantified for octave-band average values; results are presented in figure 5.2b, where ΔPSD is taken as the PSD on the storm day minus that on the previous day. Increased energy levels are observed during two periods, near 09:00 and 15:00, likely resulting from bubble impact, formation, and resonance during rainfall conditions. The periods 06:00-08:00, 10:00-14:00, and

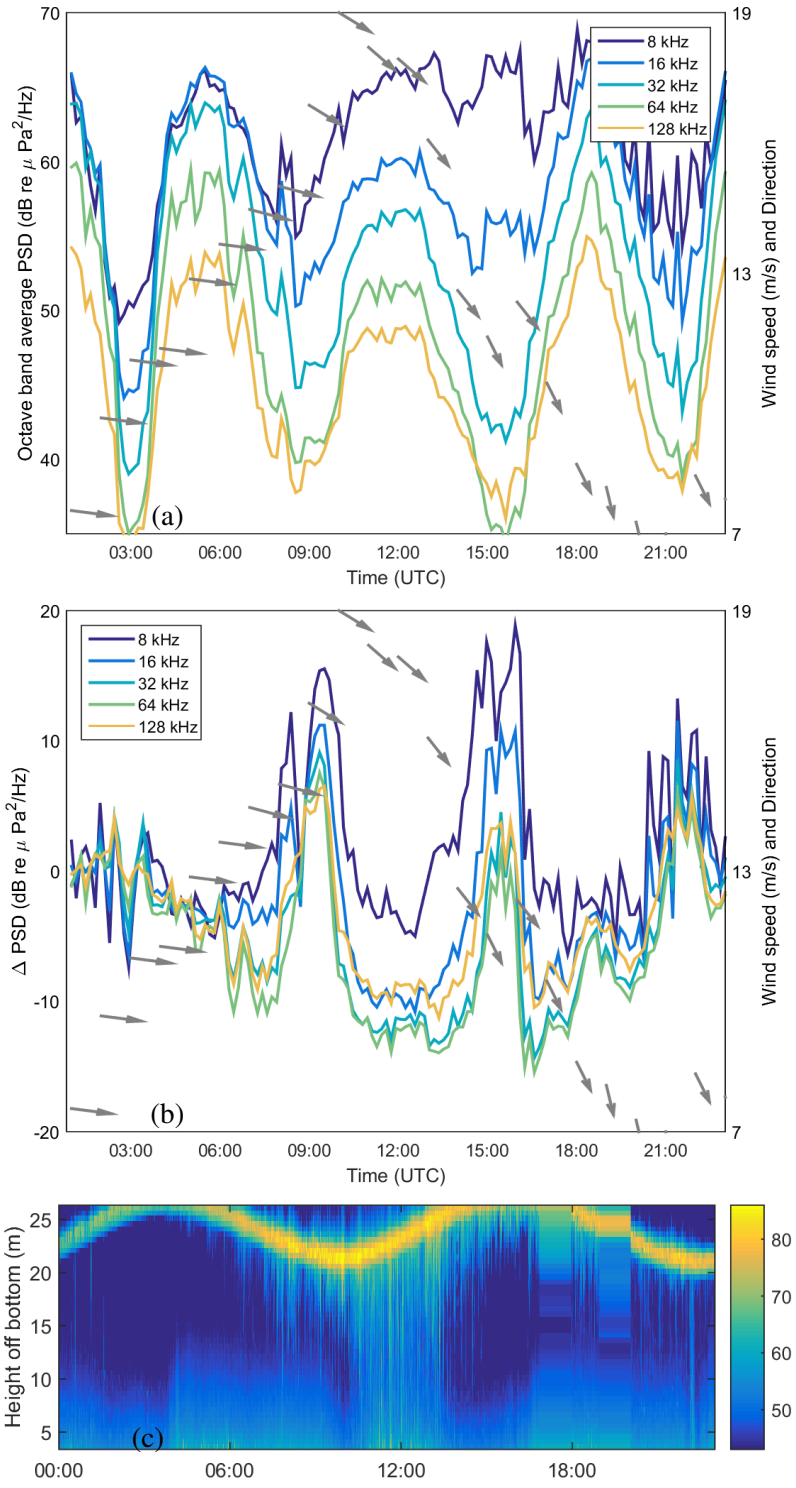

Figure 5.2: Characterization of noise level variation during storm conditions on 29 October 2015, showing a) Time series of octave-band average PSD on storm day; b) PSD difference (storm day-previous day); c) Beam-averaged ADCP backscatter intensity. The blurred sections in c) are due to missing data, where the missing data were filled in via interpolation.

16:00-20:00 show a decrease in noise levels relative to the previous day. A prolonged decrease occurs between 11:00-13:00, and is most significant in the 32 and 64 kHz bands. The minimum ΔPSD occurs at 16:34; however, this was near the high water mark, and could therefore represent variability in local sediment mobility near slack water in previous day conditions versus storm day conditions. The low ΔPSD (reduced storm day noise levels) from 12:00-13:00, by contrast, occurred during peak flood currents.

5.1.1 Reduced SGN levels

The average ΔPSD of -11 dB re μPa^2/Hz over $16 < f < 128$ kHz between 12:30-13:30 indicates significantly less SGN received at the hydrophone; this corresponds to feature (i) in figure 5.1. As previously described in section 4.3.1, high flows, and consequently active sediment transport, result in a characteristic curved SGN spectrum, during normal conditions, that does not exhibit the decrease of $f^{-5/3}$ typically reported from ocean ambient noise measurements (i.e. *Wenz*, 1962). Characteristic SGN spectra have been observed in records from low and moderate wind days, reflecting what can be considered "normal" conditions (spectra in figure 4.8 recorded in wind speeds 5-8 m/s). During high wind conditions on 29 October, however, the spectra (particularly at 12:00, 13:00, and 17:00 in figure 5.1) do not conform to the characteristic curve associated with SGN, but instead an approximately $f^{-5/3}$ power dependence on frequency.

The change in spectral slope and the decrease in noise levels occur during a period of strong NW winds and flood currents. Due to the opposing directions of tidal currents during flood tide and waves propagating into the channel from the north, wavefronts are steepened and break, and thus more energy is injected into the water column. As shown in figure 5.2c, there is a significant increase in backscatter measured at the ADCP from 12:00-13:00, and a sustained bubble plume is observed, extending to $\sim$ 15 m depth. The existence of this deep plume suggests the combination of breaking wave effects with the high turbulence levels generated by the tidal current, which acts to entrain bubbles further into the water column and can also extend a bubble's lifetime by restricting buoyant degassing processes. With a high concentration of bubbles throughout the water column, noise from bedload movement near the center of the channel (away from the hydrophone) would be subject to increased bubble scatterers compared to normal conditions, resulting in higher propagation losses and lower received levels at the hydrophone. As shown in figure 5.3, reduced sound speed in a region of high bubble concentration will lead to upward

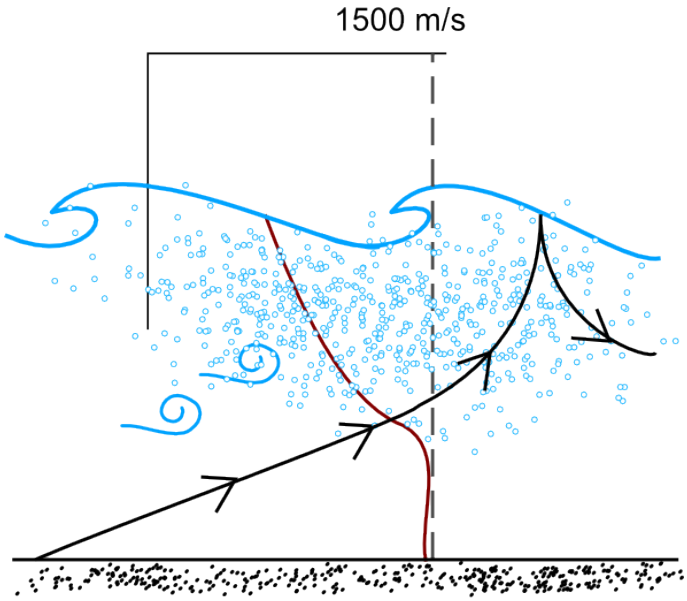

Figure 5.3: Conceptual sketch of bubble plume effects on sound propagation, indicating a sound speed profile that decreases toward the surface due to an increasing bubble concentration. A source originating near the bottom is refracted upward, resulting in the formation of a surface duct where high scatterer concentration exists.

refraction of propagating sound, introducing the possibility of a near surface duct. The sound speed is reduced at a rate related to volume concentration and bubble size (*Urick*, 1983):

$$c^{-2} = c_0^{-2} - \frac{4\pi n a}{(2\pi f)^2} \tag{5.1}$$

where c is the sound speed, n is the number of bubbles in a unit volume, and a is the bubble radius. This effect could result from bubble injection in both breaking wave and heavy rainfall conditions.

As discussed in section 2.4.3, larger bubbles typically have a shorter lifespan in the water column due to fragmentation effects (*Deane and Stokes*, 2002). Therefore, the entrained bubble population is likely of a size distribution centered at a small radius (order $<$1 mm). Given that the scattering strength peaks at resonance frequency, a bubble plume consisting of small bubbles most efficiently scatters sound at high frequencies; in addition, with the broad distribution of bubble sizes resulting from wave breaking (i.e. *Medwin and Beaky*, 1989; *Deane and Stokes*, 2002), the pronounced peak in the scattering cross section ($ka = 0.0136$) would result in elevated propagation losses over a wide bandwidth.

5.1.2 Increased noise levels due to rain

The noise level peak at 15:00 shows a sharp increase, as well as significant fluctuations, in the 8 kHz band, which would correspond to impact noise from heavy rain; this period ($\sim$14:00-16:00) aligns with the steep negative slope (feature ii) in figure 5.1. The ADCP backscatter from this timeframe (figure 5.2c) suggests the existence of a subsurface bubble layer, where intensity is significant just below the surface and falls off dramatically below $\sim$ 5m. As reported by *Ma et al.* (2005), a subsurface bubble layer has previously been found to be associated with heavy rain and/or high wind conditions.

During this two hour period, the wind speed decreased significantly from its peak of 19 m/s at 11:30, with a mean of 9 m/s from 14:00-16:00. The increase in noise levels, combined with decreasing wind speeds and backscatter that indicates high bubble concentrations near the surface, suggests that a heavy rainfall event occurred and bubbles were formed from impacting raindrops but were not entrained to depth. Consistent with the PSD curves in figure 5.1, the noise level increase occurs in the lower frequency band, with higher bands (32-128 kHz) showing little difference as compared to levels on the previous day. The lower frequency data suggest that impact noise, which is typically observed at lower frequencies compared to resonance noise (*Ma et al.*, 2005), was the dominant source over this period.

By contrast, the increased noise levels near 10:00 are observed across all frequency bands, and exhibits a more gradual peak that is sustained for several minutes. This broadband increase suggests that the rainfall characteristics (rain rate and drop size) were different than those that occurred later in the day, generating sound over a wider frequency band. The backscatter near 10:00 also shows a subsurface bubble layer during the latter half of the ebb tide, before transitioning to the deep bubble plume discussed previously. The westerly winds at this time were unlikely to result in significant wind wave formation in the Passage, due to the narrow channel geometry (figure 3.1). Therefore, the bubble layer was likely caused again by impacting raindrops.

Feature (iii) in figure 5.1, the small peaks at $\sim$50 kHz, is not well resolved in the band averaged data. These peaks occur over a narrow frequency range, and are observed in the spectra from 10:00-12:00, corresponding to the potential rainfall period described above. However, the high-frequency peaks are not observed in the second rainfall period (near 15:00). Rainfall noise at high frequency is associated with resonance from entrained

bubbles, and bubble entrainment has been found to be more likely with a particular raindrop size (*Ma et al.*, 2005). Thus, the inconsistent observation of high frequency noise peaks in storm spectra could be reflecting temporal differences in drop size during different rainfall periods.

5.1.3 High frequency noise variability

To further evaluate the trough-and-slope feature (iv), the best linear fit to the data between 68.5 and 85 kHz was calculated for the full 24 hour record on 29 October, using 1-minute average spectra. This slope estimate will be referred to as β in this document. A time series of the β values is presented in figure 5.4b, with concurrent wind speed and direction records (from the Environment Canada station at Brier Island) as well as upper 5 m average backscatter intensity. Reference lines for the Knudsen wind-driven noise spectral slope, as well as the Hinze scale, are also plotted. The Knudsen scale, which is related to noise generated by wave-formed bubbles, is significantly lower than the peak value of β. This suggests that the mechanism underlying this observed feature is different than the mechanism associated with typical wind-driven ambient noise in the ocean.

The Hinze scale represents a potential spectral slope for local acoustic energy within a breaking wave bubble plume. If bubbles are generating sound through resonance, the bubble radius range associated with this frequency range (68.5-85 kHz), via equation 2.9, is approximately 38-47 μm. For bubbles in this size range, the distribution of bubble sizes within a plume has been empirically estimated as $N(a) \propto a^{2/3}$ (*Deane and Stokes*, 2002). If it is assumed that the amplitude of resonance does not change significantly over this radius range, the energy would be expected to increase with increasing frequency, at a rate proportional to the Hinze distribution (i.e. $f^{2/3}$). As shown in figure 5.4b, the peak value of β is significantly greater than the positive Hinze-predicted slope.

The value of β is strongly correlated with wind and backscatter, suggesting that this feature is also related to bubble injection from breaking waves: backscatter levels are elevated by an increased bubble concentration, which suggests that bubbles are contributing to the observed acoustic effects. The maximum β occurs between 12:00-13:00, the same period in which noise levels show a decrease due to a high concentration of bubbles in the water column.

Figure 5.2b also shows that positive values of β generally occurred when band-averaged levels were lower than the previous day's levels, i.e. when $\Delta\text{PSD} < 0$. During the

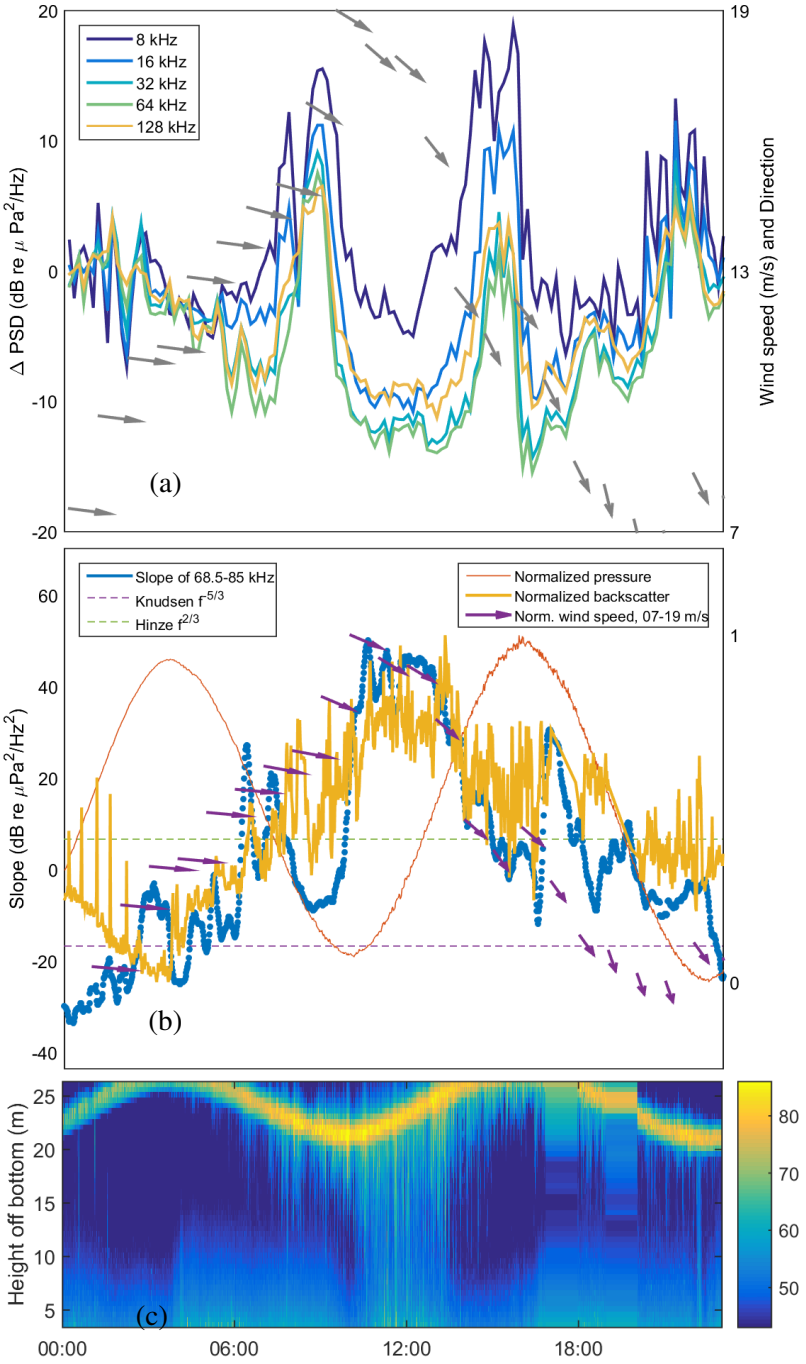

Figure 5.4: a) ΔPSD (replicate of figure 5.2b); b) Variation of high frequency slope β with wind, tide, and backscatter amplitude; c) Beam-averaged ADCP backscatter intensity (replicate of figure 5.2c). β is well correlated with depth-averaged backscatter intensity.

highest wind speeds, a steep slope occurs concurrently with a period of greatly reduced PSD levels compared to the previous day: specifically, $\beta \approx 50$ dB re μPa^2/Hz^2 and ΔPSD ≈ -18 dB re μPa^2/Hz in the band 16-128 kHz. By contrast, in periods when the trough-and-slope feature is not present (when $\beta < 0$), there is an increase in storm day noise levels compared to previous day. This again distinguishes different potential relevant mechanisms or processes: that which contributes to the feature (iv) in figure 5.1, and that which contributes to the increased noise feature (ii). The different mechanisms result in acoustic energy distributions that are distinct and exclusive; that is, increased noise at lower frequency bands is not observed at the same time as a largely positive value of β. This further points to a relationship between wave action and high-frequency noise level increases with characteristic positive slope spectral density patterns.

The β analysis was also conducted using PSD ensemble averages of 1 minute and 1 second, to evaluate the effect of averaging length on the magnitude of β, and to assess if wave-breaking events could be distinguished in a time series of 1-second average PSD estimates. The characteristics of the trough-and-slope feature were relatively unchanged when the averaging length was reduced, indicating that the feature is likely related to many events as opposed to single events.

5.2 Variability trends

The linear best-fit slope of the spectral density in the 68.5-85 kHz frequency band (β) was calculated for most of the HF2015 data record (September 2-November 21, 2015), using ten-minute averages taken at hh:00-hh:10, where hh is any hour of a given day. The wind speed and direction records are as reported from the Environment Canada weather station on Brier Island; values are recorded hourly, with wind direction in 10 degree sectors and speed in km/h. North, east, south, and west directions were defined as 315-045, 045-135, 135-225, and 225-315 degrees, respectively. A pressure time series with 1 minute sample intervals was obtained from a long-term CTD (RBR XR-420), moored near the HF2015 mooring. The times associated with high and low water marks were obtained from 5-minute averages of measured pressure. The "high/low water" period indicated on figure 5.5 was then taken as the 1 h interval centered on high/low water. Ebb and flood periods were taken as the remaining times, during decreasing or increasing pressure, respectively.

As shown in figure 5.5, the positive slope anomaly (positive β) is found over a large

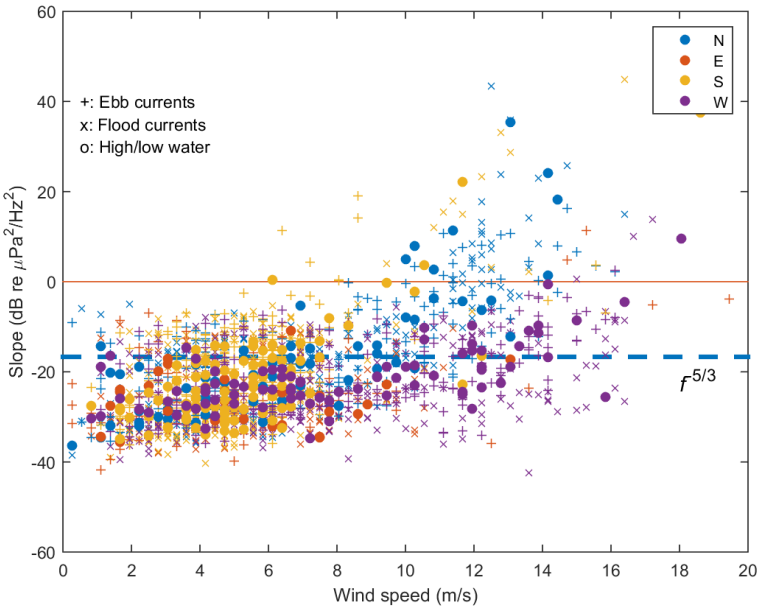

Figure 5.5: Variation of 68.5-85 kHz slope (β) with wind speed and tide, HF2015 data record, 10-minute average PSD. Wind speed data are hourly measurements from Environment Canada's Brier Island station. At low wind speeds, approximately less than 10 m/s, the trend in β is linear, centered near the Knudsen spectral slope. Above 10 m/s, β increases above zero, representing an anomalous feature for high frequency noise. The trend associated with records from low flow periods (high and low water) shows fewer positive β values compared to the records associated with either ebb or flood flows.

portion of the data record, and occurs in all flow conditions. The minimum wind speed associated with value of $\beta > 0$ is 6 m/s, which occurred during an ebb tide period with southerly (135-225 degrees) winds. Based on local geography, a SSW wind has a significant fetch, and could thus generate large wave heights; during an ebb tide, these waves are then steepened, and wavelength shortened, and thus energy injection from wave breaking is increased. In contrast, the minimum wind speed associated with $\beta > 0$ is approximately 11 m/s for a north wind and flood tide, which would also represent opposing current and wind directions but with a shorter fetch. The east and west winds show little association with positive β, where an east or west wind and $\beta > 0$ occurs only at wind speeds above 13 and 14 m/s, respectively. These directions represent cross-winds in the Passage, and would not usually generate wind waves locally. The difference in the occurrence of a positive high-frequency slope under varying wind directions highlights the influence of larger geographic characteristics on geophony within Grand Passage, and further supports the possible existence of a relationship between wave height and slope β.

5.3 Discussion

The correlation between high β and high acoustic backscatter during high wind conditions suggests that the increasing PSD at high frequency is related to the bubbles formed during breaking wave events. If the feature is related to bubble resonance, this would indicate very small bubbles, with a radius on the order of 50 μm; a 50 μm bubble resonates at approximately 65 kHz (equation 2.9). These microbubbles formed very close to the surface could resonate at a higher frequency due to their proximity to the boundary, as per the results of *Medwin and Beaky* (1989) and *Strasberg* (1953); as presented in figure 2.1, a bubble of this size could resonate at > 80 kHz within 1 m of the surface. While the bubble size distribution peak reported in the literature has been inconsistent, a peak size of 50 μm is within the reported range. Therefore, if many 50 μm bubbles are formed at the surface, the near-surface resonance would be expected at an elevated frequency (2.10) of 85-95 kHz. With downward entrainment, the resonance frequency would decrease to the natural frequency ($\approx$ 65 kHz), and pressure amplitude would decrease due to damping. The cumulative effect of such a process could create a PSD curve similar to the anomalous trough and positive slope presented in figure 5.1.

As outlined in the evaluation of a single storm day, the occurrence of high positive values of β is largely exclusive of periods in which broadband noise levels increased due to (likely heavy) rain (figure 5.2b). A possible cause of this variation and exclusivity is the effect of heavy rain on surface waves: heavy rain acts to depress wave heights (*Poon et al.*, 1992) and therefore reduce the energy in wave breaking events, which would then reduce the number of bubbles formed and could disrupt the process by which bubbles are entrained by breaking waves as additional forcing is introduced by the impacting raindrops. However, analyses of the complete dataset has indicated that positive β does occur during rain conditions. This suggests that the rate of rainfall, and raindrop size, could influence the degree to which rain affects wave-breaking bubble noise features at high frequency. Detailed rainfall rate and drop size data would be required to better examine this relationship.

CHAPTER 6

SUMMARY AND CONCLUSIONS

The soundscape in Grand Passage, Nova Scotia, has been characterized using passive acoustic datasets collected over several years from both stationary (moored) and drifting hydrophones. The characterization has identified relevant anthropophony, biophony, and geophony in the Passage, and an evaluation of the underlying mechanisms contributing to geophonic variability has been conducted. To mitigate the challenges associated with passive acoustic data collection in high flow tidal environments, and to contribute to the development of a comprehensive approach to soundscape characterization that addresses the spatial and temporal variability of the ambient noise field, several complementary measurement and analysis techniques were implemented. In addition, the research assimilated results from previous studies as well as concurrent datasets to conduct an assessment that is optimized for this particular environment.

The soundscape is significantly influenced by the high-energy flows and diverse biological and anthropogenic activity. These flows introduce low-frequency non-acoustic pseudonoise contamination that can mask acoustic signals; an evaluation of pseudonoise effects has found a strong correlation with flow speeds on time scales of hours. Biological sounds have been identified over a wide frequency range from mysticete and odontocete populations; the detection of these sounds is likely influenced by vessel noise masking and by incoherent high-frequency background noise predominantly due to mobile seabed sediments. The strong currents mobilize seabed sediments in the passage, resulting in a broadband, intense signal with tidal variability spatially correlated to seabed sediment properties. The high levels of SGN introduce constraints for detection and monitoring of

other local sounds including marine mammal vocalizations or a tidal turbine acoustic signature, but the predictable nature of the observed temporal and spatial variability provides a foundation for statistical evaluation of potential detection rates.

Storm events can influence the broadband soundscape through both generation and propagation effects, introducing additional variability that has implications for signal detection. The effects of both rainfall and high wind (wind-waves) have been evaluated, and it has been shown that significant variability in soundscape characteristics can occur during storm events: PSD increases of up to 18 dB re μPa^2/Hz, and decreases of up to -15 dB, were observed for sustained periods during a single storm event, corresponding to suggested mechanisms of heavy rain and breaking waves, respectively, for increased and decreased noise. The acoustic dataset was compared with ACDP backscatter to evaluate the changes in water column bubble concentration during a major storm. The results suggested the following relationships between sound spectra and wind/wave forcing: i) the characteristic SGN signature curve is depressed through a higher concentration of bubble scatterers in the water column due to increased breaking waves; ii) increased noise at 5-10 kHz, followed by a steep decrease as a result of heavy rain generating impact noise and forming a subsurface bubble layer that attenuates high frequencies; iii) defined PSD peaks at frequencies > 10 kHz, due to resonance of bubbles formed by impacting raindrops during medium or light rainfall conditions; and iv) a PSD minimum at ~ 68.5 kHz, followed by a PSD peak at ~ 85 kHz ("trough and slope" feature), which has been found to occur during breaking wave/high backscatter conditions.

A positive PSD slope between 68.5 and 85 kHz ($\beta > 0$) was used as a proxy for the occurrence of this feature; β was found to steepen during a period with high winds and with flow and wind directions in opposition. The minimum wind speed under which a positive β occurred was found to be 6 m/s, during a south wind and ebb tide. Southerly winds have a large fetch (from the outer Bay of Fundy), and thus wind waves could form at lower wind speeds as compared to other wind directions. This result highlights the relation between a trough-and-slope PSD feature and the presence of wind waves in Grand Passage.

The frequencies at which the steep slope characteristic occurs ($f > 65$ kHz) have not received a great deal of attention in the wind and wave noise literature. A possible explanation has been suggested in the current research, based on theoretical relations and

empirical studies of bubble size distributions; however, a conclusion has not yet been reached in the present research, and it is recommended that this unique feature be a subject of additional studies.

This research has provided important contributions toward the development of a comprehensive soundscape assessment for Grand Passage, providing baseline information upon which future soundscape measurements can be evaluated and changes identified. With consistent tidal periodicity in geophony, where band average PSD levels increase by about 20 dB re μPa^2/Hz between low flow and peak flow speeds in the 8-128 kHz bands, the detection of discrete signals in the existing soundscape can be constrained by high background levels during peak flows. This has implications for passive acoustic monitoring and assessment of marine mammal presence following turbine installation, and for detection of device noise at frequencies over 5 kHz. In the low frequency range (< 1 kHz), anthropophony introduces consistent noise with temporal variability aligning with ferry operation schedules. This could constrain detection of low frequency turbine noise or mammal sounds, particularly during ferry transit.

There exist many opportunities for additional research related to the Grand Passage soundscape, including modeling of sound propagation changes over the tidal cycle, evaluation of the shell hash contribution to SGN, and in particular, the relationship between breaking wave events and soundscape variability at high frequencies. Finally, modeling of the acoustic signature from a tidal turbine could be conducted using a selected device design and deployment location, which would provide insight into the potential acoustic impacts of tidal energy development in Grand Passage, based on the existing soundscape characterization conducted in the present research.

BIBLIOGRAPHY

Au, W. W. L., and M. C. Hastings, *Principles of Bioacoustics*, Springer, New York, NY, 2008.

Bassett, C., J. Thomson, and B. Polagye, Sediment-generated noise and bed stress in a tidal channel, *Journal of Geophysical Research: Oceans*, pp. 2249–2265, 2013.

Bendat, J. S., and A. G. Piersol, *Random data : analysis and measurement procedures*, Wiley, New York, NY, 1986.

Bharath, A., D. Groulx, and S. Campbell, Hydrophone acoustic receiver modeling: Turbulent flow modeling and acoustic analysis, *Proceedings of the 2014 COMSOL Conference*, pp. 1–7, 2015.

Cox, H., Spatial correlation in arbitrary noise fields with application to ambient sea noise, *J. Acoust. Soc. Am.*, *54*, 1289–1301, 1973.

CSR, 2014 seabed analysis - Grand Passage, Petit Passage, and Digby Gut, *Technical report*, Fundy Tidal Inc, 2014.

Deane, G. B., Surface tension effects in breaking wave noise, *J. Acoust. Soc. Am.*, *132*, 700–708, 2012.

Deane, G. B., and M. D. Stokes, Scale dependence of bubble creation mechanisms in breaking waves, *Nature*, *418*, 839–844, 2002.

Deane, G. B., and M. D. Stokes, The acoustic excitation of air bubbles fragmenting in sheared flow, *J. Acoust. Soc. Am.*, *124*, 3450–3463, 2008.

Deane, G. B., M. J. Buckingham, and C. T. Tindle, Vertical coherence of ambient noise in shallow water overlying a fluid seabed, *J. Acoust. Soc. Am.*, *102*, 3413–3424, 1997.

Deane, G. B., J. C. Priesig, and A. C. Lavery, The suspension of large bubbles near the sea surface by turbulence and their role in absorbing forward-scattered sound, *IEEE J. Oceanic Eng.*, *38*, 632–641, 2013.

Erbe, C., A. Verma, R. McCauley, A. Gavrilov, and I. Parnum, The marine soundscape of the Perth Canyon, *Prog. Oceanogr.*, *137*, 38–51, 2015.

Franz, G., Splashes as sources of sound in liquids, *J. Acoust. Soc. Am.*, *31*, 1080–1096, 1959.

Hammond, F., A. Heathershaw, and D. Langhorne, A comparison between Shields' threshold criterion and the movement of loosely packed gravel in a tidal channel, *Sedimentology*, *31*, 51–62, 1984.

Hay, A., R. Karsten, G. Trowse, D. Morin, T. Webster, J. McMillan, M. O'Flaherty-Sproul, D. Schillinger, R. Cheel, E. Marshall, N. Crowell, and K. Collins, Southwest Nova Scotia resource assessment: Final report, *Technical report*, Offshore Energy Research Association, 2013a.

Hay, A. E., J. McMillan, R. Cheel, and D. Schillinger, Turbulence and drag in a high Reynolds number tidal passage targetted for in-stream tidal power, *Oceans 2013 San Diego*, pp. 1–10, 2013b.

ISO, Acoustics - Soundscape - Part 1: Definition and conceptual framework, *ISO 12923-1:2014*, ISO/TC 43, Acoustics, Subcommittee SC 1, Noise, 2014.

Jenkins, G. M., and D. G. Watts, *Spectral analysis and its applications*, Holden-Day, San Fransisco, 1968.

Jensen, F., W. Kuperman, M. Porter, and H. Schmidt, *Computational Ocean Acoustics*, Springer Science + Business Media, New York, 2011.

Krause, B., Anatomy of the soundscape: Evolving perspectives, *J. Aud. Eng. Soc.*, *56*, 73–80, 2008.

Leighton, T., Academic Press, San Diego, CA.

Lighthill, M., The Bakerian lecture, 1961, *Proceedings of the Royal Society of London. Series A, Mathematical and Physical Sciences*, *267*, 147–182, 1962.

Lloyd, T., S. Turnock, and V. Humphrey, Modelling techniques for underwater noise generated by tidal turbines in shallow water, *Proceedings of the 30th International Conference on Ocean, Offshore and Arctic Engineering*, pp. 1–9, 2011.

Ma, B., J. Nystuen, and R. Lien, Prediction of underwater sound levels from rain and wind, *J. Acoust. Soc. Am.*, *117*, 3555–3565, 2005.

Malinka, C., In-stream tidal energy devices and marine mammals in Southwest Nova Scotia: Review of possible impacts and proposed mitigative strategies, *Technical report*, Fundy Tidal Inc., 2011.

Malinka, C., Acoustic detection ranges and baseline ambient noise measurements for a marine mammal monitoring system at a proposed in-stream tidal turbine site: Grand Passage, NS, *Honors thesis*, Dalhousie University, 2013.

Malinka, C., M. W. Brown, G. Trowse, B. Inney, and V. Zetterlind, Marine sightings report, *Technical report*, Offshore Energy Research Association, 2015a.

Malinka, C., A. Hay, and R. Cheel, Toward acoustic monitoring of marine mammals at a tidal turbine site: Grand Passage, NS, Canada, *Proc. of EWTEC 2015*, pp. 1–10, 2015b.

McMillan, J., D. Schillinger, and A. Hay, Southwest Nova Scotia resource assessment volume 3: Acoustic Doppler current profiler results, *Technical report*, Offshore Energy Research Association, 2013.

Medwin, H., and M. M. Beaky, Bubble sources of the Knudsen sea noise spectra, *J. Acoust. Soc. Am.*, *86*, 235–248, 1989.

Medwin, H., and C. Clay, *Fundamentals of Acoustical Oceanography*, Academic Press, San Diego, CA, 1998.

Medwin, H., A. Kurgan, and J. A. Nystuen, Impact and bubble sound from raindrops and normal and oblique incidence, *J. Acoust. Soc. Am.*, *88*, 413–418, 1990.

Minnaert, M., On musical air-bubbles and the sounds of running water, *Philosophical Magazine*, *16*, 235–248, 1933.

Oppenheim, A. V., R. W. Schafer, and J. R. Buck, *Discrete-Time Signal Processing*, Prentice-Hall, Upper Saddle River, NJ, 1999.

Parks, S., and P. Tyack, Sound production by north atlantic right whales (eubalaena glacialis) in surface active groups, *J. Acoust. Soc. Am.*, *117*, 3297–3306, 2005.

Parks, S., C. Clark, and P. Tyack, Short- and long-term changes in right whale calling behavior: the potential effects of noise on acoustic communication, *J. Acoust. Soc. Am.*, *122*, 3725–3731, 2007.

Polagye, B., and P. Murphy, Acoustic characterization of a hydrokinetic turbine, *Proc. of EWTEC 2015*, pp. 1–7, 2015.

Poon, Y.-K., S. Tang, and J. Wu, Interactions between rain and wind waves, *J. Phys. Oceanogr.*, *22*, 976–987, 1992.

Richards, S., E. Harland, and S. Jones, Underwater noise study supporting Scottish executive strategic environmental assessment for marine renewables, *Technical report*, Scottish Executive, Renewables and Consent Policy, 2007.

Robinson, S., and P. Lepper, Scoping study: Review of current knowledge of underwater noise emissions from wave and tidal stream energy devices, *Technical report*, The Crown Estate, 2013.

Shields, A. I., Application of similarity principles and turbulence research to bed-load movement, *Mitteilungen der preussischen versuchsanstalt fur wasserbau und schifbau*, Ott, W.P. and van Uchelen, J.C. (translators), California Institute of Technology, 1936.

Stark, N., A. E. Hay, G. Trowse, and R. Cheel, Geotechnical investigation of Grand Passage, Nova Scotia , with regard to sediment mobility and the installation of tidal energy converters, *Proc. of EWTEC 2013*, pp. 1–10, 2013.

Stimpert, A. K., W. W. L. Au, S. E. Parks, T. Hurst, and D. N. Wiley, Common humpback whale (*Megaptera Novaeangliae*) sound types for passive acoustic monitoring, *J. Acoust. Soc. Am.*, *38*, 476–482, 2013.

Strasberg, M., The pulsation frequency of nonspherical gas bubbles in liquids, *J. Acoust. Soc. Am.*, *25*, 536–537, 1953.

Strasberg, M., Nonacoustic noise interference in measurements of infrasonic ambient noise, *J. Acoust. Soc. Am.*, pp. 1487–1493, 1979.

Thomson, J., B. Polagye, V. Durgesh, and M. Richmond, Measurements of turbulence at two tidal energy sites in Puget Sound,WA (USA), *IEEE J. Ocean. Eng.*, *37*, 363–374, 2012.

Thorne, P., Laboratory and marine measurements on the acoustic detection of sediment transport, *J. Acoust. Soc. Am.*, *80*, 899–910, 1986.

Urick, R., *Principles of underwater sound*, Peninsula Publishing, Westport, CT, 1983.

Urick, R. J., *Sound Propagation in the Sea*, Department of Defense, Arlington, 1979.

Vanderlaan, A. S. M., A. E. Hay, and C. T. Taggart, Characterization of North Atlantic right-whale (*Eubalaena Glacialis*) sounds in the Bay of Fundy, *IEEE J. Oceanic Eng.*, *28*, 164–173, 2003.

Wenz, G. M., Acoustic ambient noise in the ocean: Spectra and sources, *J. Acoust. Soc. Am.*, *34*, 1936–1956, 1962.

Williams, R., E. Ashe, L. Blight, M. Jasny, and L. Nowlan, Marine mammals and ocean noise: Future directions and information needs with respect to science, policy and law in Canada, *Marine Pollution Bulletin*, *86*, 29–38, 2014.

Wu, J., Bubble flux and marine aerosol spectra under various wind velocities, *J. Geo. Res.*, *97*, 2327–2333, 1992.